On the multiscale modeling of 3D nonlinear transient magnetoquasistatic problems with emerging dynamic magnetization using the B-conforming formulation

Antoine Marteau, Innocent Niyonzima, Janne Ruuskanen, Gérard Meunier, Nicolas Galopin, Timo Tarhasaari, Paavo Rasilo, Olivier Chadebec

Computer Methods in Applied Mechanics and Engineering 458 (2026) 119042

Contents lists available at ScienceDirect

Comput. Methods Appl. Mech. Engrg.

journal homepage: www.elsevier.com/locate/cma

On the multiscale modeling of 3D nonlinear transient magnetoquasistatic problems with emerging dynamic magnetization using the B-conforming formulation

Antoine Marteau [a,b,*], Innocent Niyonzima [b], Janne Ruuskanen [c], Gérard Meunier [b], Nicolas Galopin [b], Timo Tarhasaari [d], Paavo Rasilo [d], Olivier Chadebec [b]

[a] School of Mathematics, Monash University, Clayton 3800, Victoria, Australia
[b] Univ. Grenoble Alpes, CNRS, Grenoble INP, G2Elab, F-38000 Grenoble, France
[c] Quanscient Oy, Tampere, FI-33100, Finland
[d] Tampere University, Electrical Engineering Unit, Tampere, FI-33720, Finland

ARTICLE INFO

Keywords:
Eddy currents
Heterogeneous multiscale method
Homogenization
Magnetization

ABSTRACT

This work addresses the resolution of Maxwell's equations in the magneto-quasi-static regime – or eddy currents problem – on heterogeneous geometries featuring microscopically bound currents. Assuming scale separation, the heterogeneous multiscale method (HMM) is used together with a magnetic induction (B-)conforming formulation. This formulation requires the computation of the homogenized magnetic field strength from its fine-scale distribution using different averaging techniques beyond the volume average commonly used in homogenization. This issue has only recently been studied for problems of this kind. The paper reviews the literature about the multiscale modeling of the magnetic field and magnetization, and introduces a general intuitive derivation of the homogenization of Maxwell-Ampère's equation. Six methods for the numerical upscaling of the magnetic field are also reviewed. For the first time, a B-conforming HMM formulation is validated on 3D nonlinear and transient problems. The convergence of the error introduced by using the two-scale formulation is shown numerically, and the method is used to solve a multiscale problem involving such a high number of inclusions that direct resolution is computationally impossible without homogenization.

1. Introduction

Heterogeneous materials, such as coils and magnetic cores made of laminated metal sheets or composite materials, are ubiquitous in electrical engineering. These materials are often used to create or channel the magnetic fields during electromagnetic energy conversion, while minimizing losses. Modeling these components is a major challenge, as they are the site of most energy losses, such as eddy current losses. The challenge results from the nonlinear, transient, and multiscale natures of the underlying physical phenomena.

The models for heterogeneous materials can be divided into two families. The first family leverages physical knowledge to introduce approximation of the macroscopic relation between averaged fields in specific (classes of) materials and at specific regimes, or uses (semi-)analytic models fitted with experimental data [1–3]. They often only require a few parameters and are cheap to use in

* Corresponding author.
E-mail address: antoine.marteau@monash.edu (A. Marteau).

https://doi.org/10.1016/j.cma.2026.119042
Received 2 March 2026; Received in revised form 23 April 2026; Accepted 28 April 2026
Available online 13 May 2026

simulation. However, it takes a lot of assumptions, laboratory measurements and calibrations to develop and validate these models, and their validity is difficult to control when extrapolated to similar but different materials or regimes.

The models of the second family – that some may call full field models – aim to approach the prediction of *a priori* model given by Maxwell's equations taking into account the fine-scale geometry of the heterogeneities as close as computational resources allow to. Naive predictive approaches can be prohibitively expensive and even intractable for simple real-life composites. But having accurate full field multiscale models and associated numerical methods would enable better accuracies and flexibility in simulations when needed, but could also help to develop, calibrate or extrapolate effective medium models using more simulations and fewer experiments.

This work studies the full field homogenization of general periodic materials consisting of conducting particles insulated from each other in the magneto-quasi-static (MQS) regime. Several types of methods, very often extensions of the finite element method (FEM), provide different tradeoffs between necessity of assumptions and reduction of computation cost. The Multiscale finite element method [4–7] [8, Sec. 4.2.1], and variational multiscale method combined with local orthogonal decomposition [5,9,10] are widely applicable, but their cost still increases with the number of heterogeneities.

Alternatively, the finite element heterogeneous multiscale Method (FE-HMM) [8,11,12], also known as the FE^2 in the mechanical community [13], is considered in this paper. It features a weak coupling between a macroscopic FEM problem, where the heterogeneous domain is homogenized and coarsely meshed, and several cell FEM problems. The latter account for the geometry and field behaviors at fine-scale. These problems are associated to Gauss points or elements at which the macroscopic material law is required, and are solved independently in parallel. The advantages of this method are two-fold. First, it is quite general, the main limitation being the need for an appropriate scale separation assumption. Second, its cost does not depend on the scale and number of the fine-scale features, but only on the variability of the homogenized material law across the homogenized domain and the complexity of the fine-scale behavior in one cell.

HMM was extensively used to solve linear static or time harmonic 2D problems [6,8,14–17] or 3D problems [18,19]. Magnetically nonlinear and possibly hysteretic problems were treated in 2D in [7,20–24]. Nonlinear time dependent problems were only recently tackled in 3D, using B-conforming formulation in multiharmonic regime in [25] or H-conforming formulation in transient regime in [26]. This article complements these works by studying the B-conforming formulation with a time stepping scheme. Unlike the multiharmonic method from [25], time stepping can deal with transient problems and requires solving smaller linear algebraic systems, but it is significantly less efficient for computing steady state solutions. The H-conforming approach in [26] leads to smaller systems and faster resolutions, but the convergence deteriorates with steep nonlinear magnetic law where the B-conforming approach offers more robust convergence.

The B-conforming formulation comes with the additional difficulty that one cannot always compute the homogenized magnetic field strength using a volume average. This issue was mentioned e.g., in [16,27,28], but for MQS problems, solutions were only recently studied [24,25,29,30]. As explained e.g., in [29,31], the issue arises when eddy currents confined in the conducting inclusions become strong enough to influence the average magnetic field, thus resulting in the reduction of the effective permeability of the medium.

The present work introduces a general physical explanation of the multiscale modeling of the magnetic and current density fields and shows that it is qualitatively consistent with the literature, in particular with different results in mathematical homogenization of wave scattering problems. A new numerical upscaling method is proposed and compared with four existing ones. Transient nonlinear magneto-quasi-static problems are solved in 3D, for the first time with a B-conforming formulation. A numerical validation is made against a standard fine-scale FEM formulation taking the full geometry into account, showing robustness to strong emerging dynamic magnetization. The method is applied to a problem with thousands of inclusions to illustrate its capabilities.

The paper is outlined as follows. Section 2 introduces notations for Maxwell's equations in the MQS regime and their B-conforming formulation. The review of the multiscale modeling of emerging dynamic magnetization is presented in Section 3. The two-scale and FE-HMM formulations, along with and numerical techniques for the upscaling of the magnetic field, are introduced in Section 4. Section 5 is dedicated to the experiments that numerically validate the model. Finally, conclusions are drawn in Section 6.

2. Setting and reference formulation

The modeling domain Ω, sketched in Fig. 1, consists of a heterogeneous periodic material Ω_l and a non-heterogeneous one $\Omega_{\mathrm{M}} = \Omega \backslash \Omega_l$, the interface between both is denoted by $\Gamma_{l\backslash\mathrm{M}}$. Ω_{M} is divided into air and a coil Ω_{s} fed with a current source. The interior of Ω_l is invariant by translation by a spatial vector $\boldsymbol{k}$ of magnitude l, a length smaller than the whole domain size. As a consequence, one can choose a unit cell Y generating the interior of Ω_l by translation by vectors $\boldsymbol{z_k} = (z_x k_x, z_y k_y, z_z k_z)$ where $(z_x, z_y, z_z) \in \mathbb{Z}^3$. Without loss of generality, the cell is chosen to be a cuboid[1] of diagonal $\boldsymbol{k}$. The cell is the union of an electrically conducting domain Y_{C} and nonconducting one Y_{N}. The union of all the conducting regions of Ω_l, is denoted by $\Omega_{l,\mathrm{C}}$, and the rest of the domain by $\Omega_{l,\mathrm{N}} = \Omega \backslash \Omega_{l,\mathrm{C}}$.

In this paper, it is assumed that no current can flow across Ω_l, which ensures that the homogenized domain is nonconducting. In general, this translates into the following condition inspired from [32, Section 1.1-2]: a heterogeneous domain is macroscopically conducting in a direction $\boldsymbol{v} \in \mathbb{R}^3$ if, in a periodic cell Y, there is a closed path $C \subset Y_{\mathrm{C}}$ such that $\int_C \boldsymbol{v} \cdot \boldsymbol{t} \mathrm{d}l \neq 0$, where C is still considered closed if it is Y periodic.[2]

[1] A cuboid, or rectangular hexahedron, has 6 rectangle faces, with all angles being right angles.

[2] If it has couples of endpoints p_1 and p_2 each on a face of Y of normal $\boldsymbol{e}_i$ where $i = \{x, y, z\}$, such that $p_1 = p_2 + (\boldsymbol{k} \cdot \boldsymbol{e}_i)\boldsymbol{e}_i$.

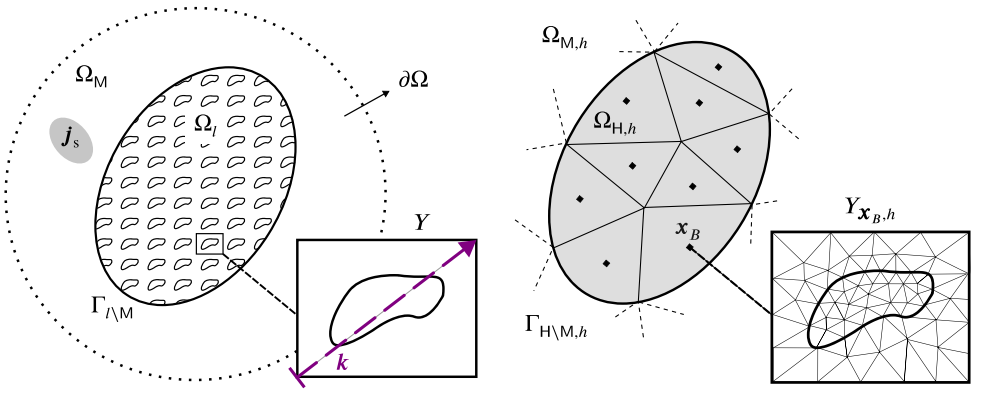

Fig. 1. A sketch of the modeling domains in our setting (left), and of the associated meshes for the macroscopic and cell problems. The outer boundary $\partial\Omega$ of the domain is not represented.

But for the sake of simplicity of the definition of cell formulation and upscaling formulas, it is further assumed that the conducting domain is strictly contained inside the cell

$$Y_{\mathrm{C}} \cap \partial Y = \emptyset, \tag{1}$$

Y_{C} does not intersect the cell boundary. The cell is said to be (electrically) insulated, the difference with more general cells of macroscopically nonconducting domain is illustrated in [30, Fig. 2.11, p83].

Other notations

Normal vector to surfaces are denoted by $\boldsymbol{n}$ and tangent vector to curves by $\boldsymbol{t}$. The discrete approximation of a domain Ω by a mesh is indicated by the $\bullet_h$ subscript as in Ω_h. The usual **grad** and **curl** conforming Sobolev spaces over Ω are respectively denoted by $H(\mathbf{grad};\Omega)$ and $\boldsymbol{H}(\mathbf{curl};\Omega)$. The space of Y-periodic **grad** conforming field is denoted by $\boldsymbol{H}^{\#}(\mathbf{grad};Y)$, and that of tangentially periodic **curl** conforming ones $\boldsymbol{H}^{\#}(\mathbf{curl};Y)$. Zero Dirichlet boundary conditions on a portion of boundary $S \subseteq \partial\Omega$ are added to the spaces as in

$$H_{0S}(\mathbf{grad};\Omega) = \left\{ v \in H(\mathbf{grad};\Omega) \;\middle|\; v|_S = 0 \right\}, \qquad \boldsymbol{H}_{\mathbf{0}S}(\mathbf{curl};\Omega) = \left\{ \boldsymbol{h} \in \boldsymbol{H}(\mathbf{curl};\Omega) \;\middle|\; \boldsymbol{h}\times\boldsymbol{n}|_S = \mathbf{0} \right\}.$$

These function spaces are discretized using first order Lagrange nodal element for $H(\mathbf{grad};)$ spaces and first order edge Nédélec elements for $\boldsymbol{H}(\mathbf{curl};)$ spaces. The resulting spaces are again denoted with a $\bullet_h$ subscript as follows: $H_{h,0S_h}(\mathbf{grad};\Omega_h)$. When it is clear from the context that the functional setting is discrete, the redundant $\bullet_h$ indices in the discrete function spaces notations will be omitted for clarity, as in $H_{h,0S}(\mathbf{grad};\Omega)$. Finally, the notation $H(\mathbf{grad};\Omega)\backslash\mathbb{R}^p$ is used to indicate that the fields are fixed to arbitrary values at p different points of Ω belonging to different connected components of Ω, this is useful to fix the gauge freedom of scalar potentials (see e.g. [33]).

Magneto-quasi-static B-conforming formulations

At low and medium frequencies, the electromagnetic fields in Ω are solution of the Magneto-Quasi-Static (MQS) Maxwell's equations in matter [34], that are defined by

$$\mathbf{curl}\,\boldsymbol{h}^l = \boldsymbol{j}^l, \quad \mathbf{curl}\,\boldsymbol{e}^l = -\partial_t \boldsymbol{b}^l, \quad \mathrm{div}\,\boldsymbol{b}^l = 0, \quad \boldsymbol{j}^l = \sigma^l \boldsymbol{e}^l, \quad \boldsymbol{h}^l = \nu^l \boldsymbol{b}^l, \quad \boldsymbol{b}^l \cdot \boldsymbol{n}|_{\Gamma_b} = 0, \quad \boldsymbol{h}^l \times \boldsymbol{n}|_{\Gamma_h} = \mathbf{0}, \tag{2}$$

where $\boldsymbol{h}^l$, $\boldsymbol{j}^l$, $\boldsymbol{e}^l$, $\boldsymbol{b}^l$, σ^l and ν^l respectively are the magnetic field strength [A/m], the electric current density [A/m^2], the electric field strength [V/m], the magnetic flux density [T], the electric conductivity [S/m] and the magnetic reluctivity [m/H]. The $\bullet^l$ superscript indicates fine-scale quantities, that are defined in the heterogeneous geometry Ω_l. The domain boundary $\partial\Omega$ is divided into Γ_b and Γ_h. The latter will be used to impose proper boundary conditions on current symmetry planes, in order to reduce the size of the modeling domain. The conductivity σ is assumed scalar, linear and only nonzero in $\Omega_{l,\mathrm{C}}$. The reluctivity in $\Omega_{l,\mathrm{C}}$ is a second-order tensor which can depend on both the magnetic field and time, and $\nu^l = \mu_0^{-1} I_3$ is set in $\Omega_{l,\mathrm{N}}$. Additionally, the standard continuity conditions of the electromagnetic at interfaces are implicitly assumed, which in particular implies $\boldsymbol{j}\cdot\boldsymbol{n}|_{\partial\Omega_{l,\mathrm{C}}} = 0$.

The B-conforming formulation uses the magnetic vector potential $\boldsymbol{a}^l$ defined in Ω and possibly the electric scalar potential v^l defined in $\Omega_{l,\mathrm{C}}$ such that

$$\boldsymbol{b}^l = \mathbf{curl}\,\boldsymbol{a}^l \quad \text{and} \quad \boldsymbol{e}^l = -\partial_t \boldsymbol{a}^l - \mathbf{grad}\, v^l. \tag{3}$$

Combining (2) and (3) leads to the following $\boldsymbol{a}$-v strong formulation:

$$\mathbf{curl}\left(\nu^l \cdot \mathbf{curl}\,\boldsymbol{a}^l\right) + \sigma^l(\partial_t \boldsymbol{a}^l + \mathbf{grad}\, v^l) = \boldsymbol{j}_{\mathrm{s}} \text{ in } \Omega, \quad \boldsymbol{a}^l \times \boldsymbol{n}|_{\Gamma_b} = \mathbf{0}, \quad \left(\nu^l \cdot \mathbf{curl}\,\boldsymbol{a}^l\right) \times \boldsymbol{n}|_{\Gamma_h} = \mathbf{0} \tag{4}$$

where the current $\boldsymbol{j}^l$ has been split into two terms, a known current source $\boldsymbol{j}_\mathrm{s}$ in Ω_s that will be imposed, and the unknown currents $\sigma(\partial_t \boldsymbol{a}^l + \mathbf{grad}\, v^l)$ in $\Omega_{l,\mathrm{C}}$. Note that the potentials $\boldsymbol{a}^l$ and v^l must be gauged as their definition (3) is not unique up to the choice of fields in the kernel of the curl for $\boldsymbol{a}^l$ (gradients) and in the kernel of the gradient for v^l (constants by connected regions). In the formulation (4), $\boldsymbol{a}^l$ has to be gauged in the full space Ω. But it is also possible to change the formulation by setting $v^l = 0$ and redefining $\boldsymbol{a}^l$ using $\boldsymbol{e}^l = -\partial_t \boldsymbol{a}^l$. In this case, $\boldsymbol{a}^l$ is called modified magnetic vector potential and does not need a gauge in $\Omega_{l,\mathrm{C}}$ anymore [35].

In this work, the tree gauge is used for the reference problem (4) and for the later macroscopic problem, and the Coulomb gauge is used for the cell problems. When using **curl**-conforming elements, the tree gauge is implemented by fixing the right amount of DoFs to zero in the discrete function space [33,36], that associated to a tree spanning the domain edges. The resulting function space is denoted by $\boldsymbol{H}_{h,\mathbf{0}_\tau}(\mathbf{curl};\Omega)$ and defined by:

$$\boldsymbol{H}_{h,\mathbf{0}_\tau}(\mathbf{curl};\Omega) := \left\{ \boldsymbol{a} \in \boldsymbol{H}_h(\mathbf{curl};\Omega) \;\middle|\; \int_{e_i} \boldsymbol{a}\cdot\boldsymbol{t} = 0 \quad \forall e_i \in \tau \right\} \tag{5}$$

where τ is a tree of edges in Ω_h and $\boldsymbol{H}_h(\mathbf{curl};\Omega)$ the chosen **curl**-conforming FEM space over Ω_h. Let also us denote by $\boldsymbol{H}_{h,\mathbf{0}_\tau,\mathbf{0}_{\Gamma_b}}(\mathbf{curl};\Omega)$ the space $\boldsymbol{H}_{h,\mathbf{0}_\tau}(\mathbf{curl};\Omega) \cap \boldsymbol{H}_{h,\mathbf{0}_{\Gamma_b}}(\mathbf{curl};\Omega)$.

Using this gauge, the weak discrete form of the reference formulation (4) reads [33,37]: find $\boldsymbol{a}^l \in \boldsymbol{H}_{h,\mathbf{0}_\tau,\mathbf{0}_{\Gamma_b}}(\mathbf{curl};\Omega)$ and $v^l \in H_h(\mathbf{grad};\Omega_{l,\mathrm{C}})\backslash\mathbb{R}^{\beta_{0,\mathrm{C}}}$ s.t.

$$\int_\Omega \boldsymbol{\nu}^l \cdot \mathbf{curl}\,\boldsymbol{a}^l \cdot \mathbf{curl}\,\boldsymbol{a}' + \int_{\Omega_{l,\mathrm{C}}} \sigma(\partial_t \boldsymbol{a}^l + \mathbf{grad}\, v^l)\cdot \boldsymbol{a}' = \int_{\Omega_\mathrm{s}} \boldsymbol{j}_\mathrm{s}\cdot\boldsymbol{a}', \quad \text{and} \quad \int_{\Omega_{l,\mathrm{C}}} \sigma(\partial_t \boldsymbol{a}^l + \mathbf{grad}\, v^l)\cdot \mathbf{grad}\, v' = 0, \tag{6}$$

for all $\boldsymbol{a}' \in \boldsymbol{H}_{h,\mathbf{0}_\tau,\mathbf{0}_{\Gamma_b}}(\mathbf{curl};\Omega)$ and $v' \in H_h(\mathbf{grad};\Omega_{l,\mathrm{C}})\backslash\mathbb{R}^{\beta_{0,\mathrm{C}}}$, where $\beta_{0,\mathrm{C}} = \beta_0(\Omega_{l,\mathrm{C}})$ is the number of connected components of $\Omega_{l,\mathrm{C}}$, that is the number of conducting inclusions. The time discretization and linearization are not detailed in (6), but the fully discretized formulation is given in Appendix A.2.

3. Multiscale modeling of the magnetic field, electric currents and magnetization

This section addresses the multiscale modeling of the magneto-quasi-static fields in the presence of strong eddy current magnetization, with a focus on magnetic field, magnetization and bound currents.

The authors argue that this requires acknowledging that confined conduction currents do not totally cancel at the macroscopic scale, but that they should instead be re-labeled as magnetization currents and eliminated from the right-hand-side of Maxwell-Ampère's equation. Based on this idea, an original and quite general derivation of the macroscopic

equations is introduced in Section 3.1. This is important for B-conforming formulations because they weakly solve for Maxwell-Ampère's equation. Keeping those magnetization currents on the right-hand side requires upscaling them, but this would be difficult due to the fact that the volume average of the eddy currents over any conducting inclusion vanishes.

Our derivation is then compared, and shown to be consistent with, existing approaches to the homogenization of Maxwell's equations that consider the emergence of additional magnetization due to confined currents. Comparison with classical approaches is made in Section 3.2, and with more recent mathematical approaches in Section 3.3. The state of the art is reviewed after giving our derivation because notations and concepts that are rarely directly discussed in the literature are introduced, such as the fine-scale distribution of the magnetization emerging from the fine-scale currents, denoted by $\boldsymbol{m}_{l\to\mathrm{H}}$.

3.1. On the scale dependency of the definition of the electromagnetic fields in matter

The general Maxwell-Ampère's law in matter [34, Eq. (7.43.iv) & (7.51)] reads

$$\mathbf{curl}\left(\frac{1}{\mu_0}\boldsymbol{b}\right) = \boldsymbol{j} + \boldsymbol{j}_\mathrm{m} + \boldsymbol{j}_\mathrm{p} + \epsilon_0 \partial_t \boldsymbol{e} \tag{7}$$

with $\boldsymbol{j}$ the conduction currents, $\boldsymbol{j}_\mathrm{m} = \mathbf{curl}\,\boldsymbol{m}$ the magnetization currents, $\boldsymbol{j}_\mathrm{p} = \partial_t \boldsymbol{p}$ the polarization currents and $\epsilon_0\partial_t\boldsymbol{e} + \boldsymbol{j}_\mathrm{p} = \partial_t(\boldsymbol{p} + \epsilon_0\boldsymbol{e}) = \partial_t \boldsymbol{d}$ the displacement currents. Under the magneto-quasi-static approximation, displacement currents disappear and Maxwell-Ampère's law in matter is obtained by defining $\boldsymbol{h} = \mu_0^{-1}\boldsymbol{b} - \boldsymbol{m}$. Re-arranging the terms of (7) leads to the equivalent equations

$$\mathbf{curl}\left(\frac{1}{\mu_0}\boldsymbol{b}\right) = \boldsymbol{j} + \boldsymbol{j}_\mathrm{m} \qquad \Longleftrightarrow \qquad \mathbf{curl}\Big(\underbrace{\frac{1}{\mu_0}\boldsymbol{b} - \boldsymbol{m}}_{\boldsymbol{h}}\Big) = \boldsymbol{j}. \tag{8}$$

Let us examine how this relation behaves in the problem at hand (4). The fields defined at the scale of the inclusion are written using lowercase letters, and the fields defined at the macroscopic scale using capital letters. Some (induced) conduction currents $\boldsymbol{j}^l = \sigma^l \boldsymbol{e}^l$ are considered in the conducting inclusion, and some magnetization of the matter may be taken into account in the magnetic permeability linking $\boldsymbol{b}^l$ and $\boldsymbol{h}^l$. So (8) at scale l reads

$$\mathbf{curl}\left(\frac{1}{\mu_0}\boldsymbol{b}^l\right) = \boldsymbol{j}^l + \boldsymbol{j}^l_\mathrm{m} \qquad \Longleftrightarrow \qquad \mathbf{curl}\Big(\underbrace{\frac{1}{\mu_0}\boldsymbol{b}^l - \boldsymbol{m}^l}_{\boldsymbol{h}^l}\Big) = \boldsymbol{j}^l. \tag{9}$$

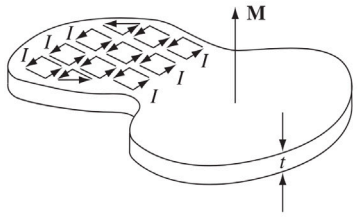

FIGURE 6.15

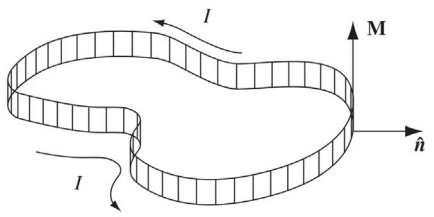

FIGURE 6.16

Fig. 2. Figures from [34, Sec. 6.2.2] illustrating how confined current loops result in macroscopic bound current and the associated magnetization. The author explains that the fine-scale currents do not disappear because they form small loops, but because currents of locally adjacent loops go the opposite direction. However, this cancelling does not happen at the boundary of the material or when neighboring loops have different intensities.

where it is always possible to compute $\boldsymbol{m}^l = \mu_0^{-1}\boldsymbol{b}^l - \boldsymbol{h}^l$ and then compute $\boldsymbol{j}^l_{\mathrm{m}} = \mathbf{curl}\,\boldsymbol{m}^l$ from $\boldsymbol{b}^l$ and $\boldsymbol{h}^l$.

Now, let us consider the heterogeneous domain Ω_l as a homogeneous material Ω_{H}. Denote by $\boldsymbol{j}^l_{\mathrm{b}}$ the free currents confined at scale l, i.e. those that do not flow across Ω_l but instead loop in a compact support included in one geometric period. In this paper, the inclusions are insulated so all currents are confined: $\boldsymbol{j}^l_{\mathrm{b}} = \boldsymbol{j}^l$. For such problems, Ω_{H} is always modeled with a zero conductivity, and Maxwell-Ampère's equation reduces to $\mathbf{curl}\,(\boldsymbol{H}) = \mathbf{0} = \boldsymbol{J}$.

Assume the existence of a field averaging operator $\langle\,\rangle$ that smoothes the fields to yield their macroscopic counterpart while preserving the differential equations between fields. In practice, the existence of $\langle\,\rangle$ requires suitable scale separation assumptions. This operator must be linear and be the identity for constant fields. However, we *refrain* from assuming that $\langle \boldsymbol{j}^l_{\mathrm{b}} \rangle = \mathbf{0}$, following the physical intuition that homogenizing does not cancel confined current everywhere at the macroscopic scale as illustrated in Fig. 2. Instead, the currents $\langle \boldsymbol{j}^l_{\mathrm{b}} \rangle$ are considered to be macroscopic magnetization currents and denoted by $\boldsymbol{J}_{\mathrm{m},l\to\mathrm{H}}$, where the subscript $\bullet_{l\to\mathrm{H}}$ indicates that these currents are free at scale l but bound at the macroscopic scale. Furthermore, let $\boldsymbol{J}_{\mathrm{m},\bullet\to l} = \langle \boldsymbol{j}^l_m \rangle$ denote the homogenized *magnetization-currents-at-the-scale-l*, and $\boldsymbol{M}_{\bullet\to l} = \langle \boldsymbol{m}^l \rangle$ the homogenized *magnetization-at-the-scale-l*. Applying $\langle\,\rangle$ to (9) leads to the macroscopic equations

$$\mathbf{curl}\left(\frac{1}{\mu_0}\boldsymbol{B}\right) = \underbrace{\mathbf{0}}_{\boldsymbol{J}} + \underbrace{\boldsymbol{J}_{\mathrm{m},\bullet\to l} + \boldsymbol{J}_{\mathrm{m},l\to\mathrm{H}}}_{\boldsymbol{J}_{\mathrm{m}}} \quad\Longleftrightarrow\quad \mathbf{curl}\Big(\underbrace{\frac{1}{\mu_0}\boldsymbol{B} - \overbrace{\left(\boldsymbol{M}_{\bullet\to l} + \boldsymbol{M}_{l\to\mathrm{H}}\right)}^{\boldsymbol{M}}}_{\boldsymbol{H}}\Big) = \underbrace{\mathbf{0}}_{\boldsymbol{J}} \quad \text{in } \Omega_{\mathrm{H}}, \tag{10}$$

where $\boldsymbol{B} = \langle \boldsymbol{b}^l \rangle$ and the term $\boldsymbol{M}_{l\to\mathrm{H}}$ such that $\mathbf{curl}\,\boldsymbol{M}_{l\to\mathrm{H}} = \boldsymbol{J}_{\mathrm{m},l\to\mathrm{H}}$ was introduced but is yet undefined. Here, a definition for a magnetic field $\boldsymbol{m}_{l\to\mathrm{H}}$ related to $\boldsymbol{j}^l_{\mathrm{b}}$ would be enough to determine how to homogenize (9) into (10). Indeed, if $\mathbf{curl}\,\boldsymbol{m}_{l\to\mathrm{H}} = \boldsymbol{j}^l_{\mathrm{b}}$, then $\boldsymbol{m}_{l\to\mathrm{H}}$ determines $\boldsymbol{j}^l_{\mathrm{b}}$, $\boldsymbol{J}_{\mathrm{m},l\to\mathrm{H}}$ and $\boldsymbol{M}_{l\to\mathrm{H}} = \langle \boldsymbol{m}_{l\to\mathrm{H}} \rangle$. Additionally, $\boldsymbol{H}$ can be directly homogenized from $\boldsymbol{h}^l$ and $\boldsymbol{m}_{l\to\mathrm{H}}$ using

$$\boldsymbol{H} = \frac{1}{\mu_0}\boldsymbol{B} - \boldsymbol{M}_{\bullet\to l} - \boldsymbol{M}_{l\to\mathrm{H}} = \frac{1}{\mu_0}\langle \boldsymbol{b}^l \rangle - \langle \boldsymbol{m}^l \rangle - \langle \boldsymbol{m}_{l\to\mathrm{H}} \rangle = \left\langle \frac{1}{\mu_0}\boldsymbol{b}^l - \boldsymbol{m}^l - \boldsymbol{m}_{l\to\mathrm{H}} \right\rangle = \langle \boldsymbol{h}^l - \boldsymbol{m}_{l\to\mathrm{H}} \rangle. \tag{11}$$

To define $\boldsymbol{m}_{l\to\mathrm{H}}$, assume $V_{\mathrm{C}} \subset \Omega_l$ is a simply connected compact domain[3] of diameter $\simeq l$ and assume that if some $\boldsymbol{j}^l_{\mathrm{b}}$ flows inside V_{C} then it is confined inside, that is $\boldsymbol{j}^l_{\mathrm{b}} \cdot \boldsymbol{n}|_{\partial V_{\mathrm{C}}} = 0$. Then there exist $\boldsymbol{m}_{l\to\mathrm{H}} \in \boldsymbol{H}(\mathbf{curl}; V_{\mathrm{C}})$ such that

$$\mathbf{curl}\,\boldsymbol{m}_{l\to\mathrm{H}} = \boldsymbol{j}^l_{\mathrm{b}} \text{ in } V_{\mathrm{C}}, \qquad \boldsymbol{m}_{l\to\mathrm{H}} \times \boldsymbol{n} = \mathbf{0} \text{ on } \partial V_{\mathrm{C}}. \tag{12}$$

The boundary condition ensures that the only source of $\boldsymbol{m}_{l\to\mathrm{H}}$ are the currents confined in V_{C}, in the sense that $\boldsymbol{j}^l_{\mathrm{b}}|_{V_{\mathrm{C}}} = \mathbf{0} \Rightarrow \int_{V_{\mathrm{C}}} \boldsymbol{m}_{l\to\mathrm{H}} = \mathbf{0}$.[4] The figure 1 in [24] gives a 2D example of a $\boldsymbol{m}_{l\to\mathrm{H}}$ (named $\boldsymbol{t}_0$ there). Also, the paper proposes a justification and generalization of (12) for conducting domain that are not insulated, using a Helmholtz decomposition.

This definition of $\boldsymbol{m}_{l\to\mathrm{H}}$ seems to require strong assumptions: the a priori knowledge of volumes V_{C} containing any current loop of diameter small in front of the characteristic size of the macroscopic scale. However, multiscale methods assuming scale separation always require such strong hypotheses. Most papers using FE-HMM usually assume that the conducting domain is an insulated inclusion, which is a stronger hypothesis. This is the case of our problem (4), for the rest of the paper, $V_{\mathrm{C}} = Y_{\mathrm{C}}$ is assumed.

To sum up, the two key ingredients in this derivation are:

- an upscaling operator that preserves differential equations, and
- the knowledge of fine-scale volumes enclosing the fine-scale current loops.

[3] Assuming simple connectedness does not reduce generality. If a compact but not simply connected $\tilde{V}_{\mathrm{C}}$ is known, define V_{C} as the convex hull of $\tilde{V}_{\mathrm{C}}$ which makes it simply connected without increasing the diameter.

[4] Further, one can show that adding the gauge condition $\mathrm{div}\,\boldsymbol{m}_{l\to\mathrm{H}} = 0$ in V_{C} is enough to uniquely determine $\boldsymbol{m}_{l\to\mathrm{H}}$ and have $\boldsymbol{j}^l_{\mathrm{b}}|_{V_{\mathrm{C}}} = \mathbf{0} \Rightarrow \boldsymbol{m}_{l\to\mathrm{H}} = \mathbf{0}$.

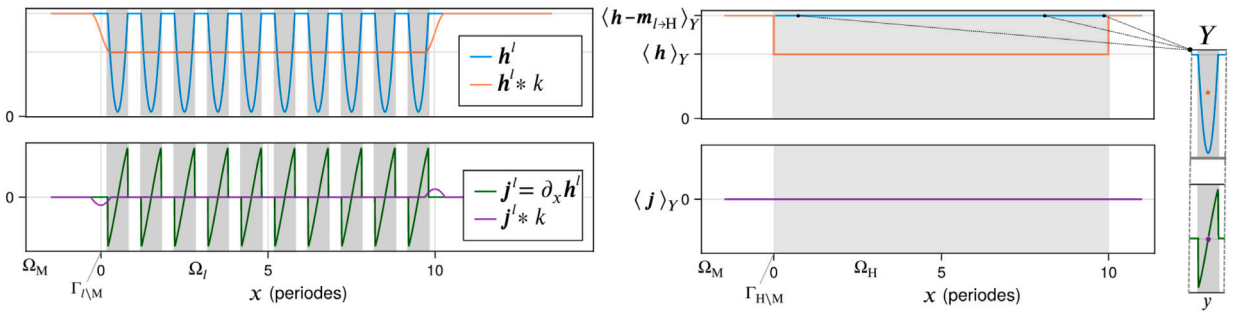

Fig. 3. Left: illustration of the magnetic field and currents in a 1D heterogeneous material. The Maxwell-Ampère's law reduces to $\partial_x \boldsymbol{h}^l = \boldsymbol{j}^l$ in the inclusions, and $\partial_x \boldsymbol{h}^l = 0$ in air. Additionally, the constraint $\int_{Y_{\mathrm{C}}} \boldsymbol{j}^l(y)\mathrm{d}y = 0$ – induced currents are confined – implies that $\boldsymbol{h}^l$ is constant in the nonconducting domains, and that the fields are perfectly periodic in Ω_{H}. Using a convolution with the cell average smoother, the smoothed field are constant in Ω_l but a jump of magnetic field associated with nonzero currents $k * \boldsymbol{j}^l$ appear at $\Gamma_{l\backslash\mathrm{M}}$.
Right: solution of the associated two-scale problem, assuming that a correct scaling of the material parameter ensures that the original cell current are preserved in each cell. The macroscopic current (cell average of the two-scale limit of the current) is zero in all cells, so $\langle \boldsymbol{j} \rangle_Y = 0$ in Ω. Also, cells at all points $x \in \Omega_{\mathrm{H}}$ actually have identical solutions. But the average of the two-scale limit of $\boldsymbol{h}^\epsilon$ is not constant at $\partial\Omega_{\mathrm{H}}$, so $\partial_x \langle \boldsymbol{h} \rangle_Y \neq \langle \boldsymbol{j} \rangle_Y$ at $\Gamma_{l\backslash\mathrm{M}}$.
In higher dimension, the behavior happening at $\partial\Omega_{\mathrm{H}}$ would also appear inside Ω_{H} because different inclusions will have confined currents of different intensity, leading to $\partial_x \langle \boldsymbol{h} \rangle_Y \neq \langle \boldsymbol{j} \rangle_Y$ inside Ω_{H}.

This allows to define the magnetic field associated with the confined currents via (12) in order to relabel both of them as magnetization fields at the macroscopic scale. Eq. (12) is thus the key definition that fully determines (10) and (11). These preserve the physical definition of the fields in Maxwell-Ampère's equation, that is the free currents are conduction currents with charges physically following the current flow, and the rest are bound currents. In the next paragraphs, this rather intuitive derivation is compared with different approaches, uncovering a number of similarities with it.

3.2. Classical homogenization

The classical way of justifying the homogenization of Maxwell's equations [38, p. 134–140] [39,40], in particular the definition of Maxwell's equations in matter, uses a pointwise volume average in a small neighborhood $V_{\boldsymbol{x}}$ of $\boldsymbol{x}$ such that $\tilde{\boldsymbol{H}}(x) = |V_{\boldsymbol{x}}|^{-1} \int_{V_{\boldsymbol{x}}} \boldsymbol{h}(\boldsymbol{y}) d\boldsymbol{y}$. This is actually equivalent to defining the homogenized field as the convolution of $\boldsymbol{h}$ with a smoothing function $k(\boldsymbol{x}) = \mathbb{1}_{V_{\boldsymbol{0}}}(\boldsymbol{x})\, |V_{\boldsymbol{0}}|^{-1}$ where $V_{\boldsymbol{0}}$ is the neighborhood centered on $\boldsymbol{0}$ and $\mathbb{1}_V$ is the indicator function of the domain V. Indeed,

$$|V(\boldsymbol{x})|^{-1} \int_{V_{\boldsymbol{x}}} \boldsymbol{h}(\boldsymbol{y}) d\boldsymbol{y} = \int_{\mathbb{R}^3} \mathbb{1}_{V_{\boldsymbol{0}}}(\boldsymbol{x} - \boldsymbol{y})\, |V_{\boldsymbol{0}}|^{-1} h(\boldsymbol{y}) d\boldsymbol{y} = \int_{\mathbb{R}^3} k(\boldsymbol{x} - \boldsymbol{y}) h(\boldsymbol{y}) d\boldsymbol{y} = (k * \boldsymbol{h})(\boldsymbol{x}), \qquad \text{so } \tilde{\boldsymbol{H}} = k * \boldsymbol{h}.$$

If the smoother k is chosen to be a mollifier,[5] the convolution commutes with derivatives, so smoothing preserves the Maxwell equations [14,39,40], making $\boldsymbol{h} \to k * \boldsymbol{h}$ a suitable averaging operator $\langle\,\rangle$ for the earlier derivation. For example,

$$\mathbf{curl}\, \boldsymbol{h} = \boldsymbol{j} \quad \Rightarrow \quad k * (\mathbf{curl}\, \boldsymbol{h}) = k * \boldsymbol{j} \quad \Leftrightarrow \quad \mathbf{curl}\, (k * \boldsymbol{h}) = k * \boldsymbol{j} \quad \Leftrightarrow \quad \mathbf{curl}\, \tilde{\boldsymbol{H}} = \tilde{\boldsymbol{J}}. \tag{13}$$

Although $\tilde{\boldsymbol{H}}$ and $\tilde{\boldsymbol{J}}$ are smooth macroscopic fields such that $\mathbf{curl}\, \tilde{\boldsymbol{H}} = \tilde{\boldsymbol{J}}$, they are not the fields that appear in the usual Maxwell-Ampère's equations in matter because $\tilde{\boldsymbol{J}}$ contains all currents, not only the free/conduction currents.

Nonetheless, convolutions are a great tool to compute and visualize what homogenized fields fulfilling Maxwell's equations could look like. A 1D example is given in Fig. 3. It corresponds to a stack of ten laminated infinite magnetic sheets, immersed in a homogeneous magnetic field parallel to the sheets, a classic setting described e.g. in [41] and similar to [23, Fig. 6]. In this setup, it is known that the magnetic field is constant outside the conducting domain. As a result, $\boldsymbol{h}$ has to be constant in $\Omega_{l,\mathrm{N}}$, as well as $\boldsymbol{H}$ in $\Omega_{\mathrm{M}} \cup \Omega_{\mathrm{H}}$. Additionally, the exact same behavior happens in each spatial period of Ω_l and periodic cell Y, even if considering nonlinear and hysteretic $\boldsymbol{\nu}$ in $\Omega_{l,\mathrm{C}}$, which should make this problem simple to homogenize. This example shows how the smoothed confined currents $\boldsymbol{j}^l * k$ do not cancel completely, although no macroscopic free currents are expected.

Authors using convolutions invoke physical arguments [38] or multipole series expansion [39,40] in order to differentiate between macroscopic magnetization currents and free currents. But the equations were not used in the context of numerical multiscale modeling, they are likely not quantified precisely enough for this. Convolutions have also been used to informally derive homogenized models for electromagnetic problems [14,15], although the emergence of additional magnetization is not considered.

[5] A mollifier is a positive C^∞ function of integral 1 and that is zero outside a compact support. An example is $\boldsymbol{x} \to \left(\exp\left(\frac{-1}{1-|\boldsymbol{x}|^2}\right) \text{ if } \|\boldsymbol{x}\| < 1, \text{ else } 0\right)$, its support is the ball of radius 1. The term comes from the distribution theory.

While averaging via convolution provides useful insights, it requires full knowledge of the l-scale field distributions and does not help the mathematical study of numerical homogenization methods. For this purpose, asymptotic homogenization and analytical multiscale modeling techniques are necessary.

3.3. Mathematical multiscale modeling

This section is restricted to models considering two scales only. The goal of the two-scale modeling is to approximate the problem at hand by strongly splitting the variation of the fields between a fine-scale and a coarse (or macroscopic) scale. This is achieved assuming a scale separation assumption, that often relates to the ratio of the characteristic size of fine-scale features and the size of the whole heterogeneous domain, in our case l and H respectively. More precisely, such derivations follow the following methodology

$$\boldsymbol{h}^l(\boldsymbol{x}) \text{ in } \Omega_l \xrightarrow{\text{embedding}} \boldsymbol{h}^\epsilon(\boldsymbol{x}) \text{ in } \Omega_\epsilon \xrightarrow[\epsilon\to 0]{\text{convergence}} \begin{cases} \boldsymbol{h}(\boldsymbol{x},\boldsymbol{y}) \text{ in } \Omega_{\mathrm{H}} \times Y \\ (\text{ and } \boldsymbol{H}(\boldsymbol{x}) \text{ in } \Omega_{\mathrm{H}}) \end{cases} \xrightarrow[\text{(FE-HMM here)}]{\text{discretization}} \begin{cases} \boldsymbol{h}(\boldsymbol{y}) \text{ in } Y_h(\boldsymbol{x}_B), \forall B \\ \boldsymbol{H}(\boldsymbol{x}) \text{ in } \Omega_{\mathrm{H},h}. \end{cases} \tag{14}$$

The problem at hand is embedded in a sequence of problems indexed by a parameter ϵ which is the ratio between the heterogeneities/inclusion size and the diameter of the heterogeneous material. Then, it is shown that the sequence of problems and of their solutions – e.g. $\boldsymbol{h}^\epsilon$ – converge in some sense[6] to a limit problem as ϵ tends to zero. The two-scale solutions are two-scale fields $\boldsymbol{h}(\boldsymbol{x},\boldsymbol{y})$ for $\boldsymbol{x},\boldsymbol{y} \in \Omega_{\mathrm{H}} \times Y$ where $\boldsymbol{h}$ is Y-periodic in $\boldsymbol{y}$. Macroscopic and cell problems are then derived from the two-scale formulation, the macroscopic fields that are solution being defined by Y-averages such as $\boldsymbol{B}(\boldsymbol{x}) = \langle\, \boldsymbol{B}(\boldsymbol{x},\boldsymbol{y})\,\rangle_Y$ for all $\boldsymbol{x} \in \Omega_{\mathrm{H}}$. Finally, the two-scale problem is discretized for the numerical approximation, for example using the FE-HMM method.

In the example on the right of Fig. 3, it is assumed that there is a two-scale problem with solutions (e.g. $\boldsymbol{h}$ and $\boldsymbol{j}$) coinciding in every cell with the original field in any geometric period of Ω_l ($\boldsymbol{h}^l$ and $\boldsymbol{j}^l$), which is a very mild assumption for this problem. However, the cell average used for upscaling cancels all the currents, but not the magnetic field associated with the current. As a consequence, the macroscopic current $\langle \boldsymbol{j} \rangle_Y$ is not the curl of the macroscopic two-scale limit of $\langle \boldsymbol{h} \rangle_Y$. So the two-scale convergence combined with average $\langle\ \rangle_Y$ do not exactly preserve differential equations, and $\boldsymbol{H}$ cannot be $\langle \boldsymbol{h} \rangle_Y$ if it is required that $\boldsymbol{J} = \boldsymbol{0}$.

In the context of MQS problems, the methodology (14) has been employed and/or numerically validated for example in [6–8,16,20–26,44,45]. We refer to [23,26] for a broader literature on other homogenization approaches used for this problem.

The embedding step of (14) usually leverages a nondimensionalization and renormalization of each quantity appearing in the equations in order to define characteristic quantities [23]. In general, these quantities inform on the balance between the different term of the equations, enabling for example to remove negligible terms like the displacement currents [33]. In homogenization, such study is crucial in order to determine correctly the homogenized equations, especially when they differ from the fine-scale ones. Indeed, the limit problem is not only determined by the equations of the original problem, but also by the scaling assumptions made on the different terms when embedding the problem in the ϵ-indexed problem sequence.

Linear electromagnetic wave scattering problems are studied in [46,47] with application to geophysics in mind. Different possible ϵ scalings are introduced in order to preserve how different characteristic quantities compare to each other as $\epsilon \to 0$, leading to different two-scale problems and different equations for the cell and macroscopic problems. Strictly positive conductivity is assumed everywhere in the heterogeneous domain, and frequency dependent permittivity and conductivity are derived. However, although the authors mention that the permeability needs to be frequency dependent in some cases [46, Remark 5], no explicit formulas for frequency dependent homogenized permeability[7] or upscaling of $\boldsymbol{H}$ is given, so these papers do not directly address the problem posed by the emergence of magnetization in B-conforming formulations.

Other studies of linear scattering problems for application to meta-materials do identify so-called *artificial magnetism* phenomenon predicted by e.g. [27]. This phenomenon is often obtained using a $\sim\epsilon^{-2}$ scaling of the electric permittivity in the inclusions, and $\sim$1 scaling in the matrix/insulator [10,48–54]. This scaling is chosen to preserve the *optical diameter* of the inclusions according to [48]. In [49,55], the diameter of the inclusions scale differently than the distance between them. [32] considers infinite permittivity. Alternatively, a scaling $\sim \epsilon^{-1}$ of the surface electric conductivity of conducting inclusion boundaries is used in [31] in order to preserve the electromotive force around the inclusion [31, Sec. 1.2]. A $\sim\epsilon^{-2}$ scaling of the bulk conductivity of the inclusion is used in [56]. We conjecture that a similar scaling should be used for problem (4).

The derivation (10)–(11)–(12) above is consistent in several ways with these results. The artificial magnetism is precisely the emergence of macroscopic magnetization due to confined current impacting the homogenized permeability. The analogy of merging bound current loops is mentioned in [49,55] to explain the discontinuity of $\langle \boldsymbol{h} \rangle_Y$ at the homogenized domain boundary. The third correction term for $\boldsymbol{h}$ in [52, Th. 3.1], denoted by $\boldsymbol{u}_3$, is similar to $\boldsymbol{m}_{l\to\mathrm{H}}$ defined above with the specific gauge $\operatorname{div}\boldsymbol{m}_{l\to\mathrm{H}} = \operatorname{div}\boldsymbol{h}$. Indeed, it is a curl conforming field with zero tangential trace on the boundary of the inclusion Y_{C} (their Σ), and such that $\boldsymbol{h}(\boldsymbol{x},\boldsymbol{y}) = \boldsymbol{H}(\boldsymbol{x}) + \boldsymbol{u}_3(\boldsymbol{y})$ in Y_{C}, so $\mathbf{curl}\,\boldsymbol{u}_3$ accounts for all the currents in the inclusion. But the relation $\boldsymbol{h} = \boldsymbol{H} + \boldsymbol{u}_3$ in Y_{C} excludes the volume average of $\langle \boldsymbol{u}_3 \rangle_Y$ from $\boldsymbol{H}$ by definition. Similarly, the h_i^1 term in [31, Eq. (15)] also seems to correspond to $\boldsymbol{m}_{l\to\mathrm{H}}$ in the same way.

[6] The convergence in the two-scale sense [42,43] is frequently used for elecromagnetism problems.

[7] In [46,47], constant homogenized permeability resulting from solving magnetostatic cell problems are derived in some cases [47, Eq. (32)-(33)]. In another case, an infinite permeability is obtained [47, Eq. 73].

Finally, some aforementioned papers define $\boldsymbol{H}$ explicitly in terms of the two-scale limit $\boldsymbol{h}$ of $\boldsymbol{h}^\epsilon$, but never as the volume average $\langle \boldsymbol{h} \rangle_Y$. Pendry et al. [27] may have been the first to suggest upscaling the magnetic field using the following edge tangential average $\langle\, \rangle_{\boldsymbol{\gamma}_Y}$ defined by

$$\boldsymbol{h} \to \langle \boldsymbol{h} \rangle_{\boldsymbol{\gamma}_Y} := \begin{bmatrix} \frac{1}{4k_x} & 0 & 0 \\ 0 & \frac{1}{4k_y} & 0 \\ 0 & 0 & \frac{1}{4k_z} \end{bmatrix} \cdot \int_{\boldsymbol{\gamma}_Y} (\boldsymbol{h} \cdot \boldsymbol{t}) \boldsymbol{t} \, \mathrm{d}l, \tag{15}$$

where $\boldsymbol{\gamma}_Y$ consists of the twelve edges of Y. Each component of the vector resulting from the integration is normalized by the total length of the four parallel cell edges in its direction. This average is used in the multiscale modeling derivation in [31], detailing both its mathematical and physical justification. An alternative definition, called *geometric average*, is developed in [50]. It is equivalent to (15) when $\boldsymbol{y} \to \boldsymbol{h}(\boldsymbol{x}, \boldsymbol{y})$ is Y-periodic and the high conductivity region is insulated (1). In fact, the path average of $\boldsymbol{h}$ on homeomorphic Y-periodic paths – e.g. parallel cell edges – is an invariant, a visual proof is given in [30, Fig. 2.12]. Physically, each invariant is the magnetomotive force between the faces joined by the path. The invariants for the three equivalent classes of such path in the periodized cell[8] define the three components of $\boldsymbol{H}$, after normalizing by the distance between the faces (the length of the normal edge). The edge and geometric averages are consistent with (11). Indeed, it can be shown [30, Eq. (2.81)] that

$$\boldsymbol{h}_{\mathrm{p}} \in \boldsymbol{H}^{\#}(\mathbf{curl}; Y) \quad \text{and} \quad \mathbf{curl}\, \boldsymbol{h}_{\mathrm{p}} = \boldsymbol{0} \text{ in } Y \qquad \Longrightarrow \qquad \left\langle \boldsymbol{h}_{\mathrm{p}} \right\rangle_Y = \left\langle \boldsymbol{h}_{\mathrm{p}} \right\rangle_{\boldsymbol{\gamma}_Y}. \tag{16}$$

If one extends $\boldsymbol{m}_{l\to \mathrm{H}}$ by $\boldsymbol{0}$ in Y_{N}, the field $\boldsymbol{h} - \boldsymbol{m}_{l\to \mathrm{H}}$ satisfies both conditions. Further, $\langle \boldsymbol{m}_{l\to \mathrm{H}} \rangle_{\boldsymbol{\gamma}_Y} = \boldsymbol{0}$ because $\boldsymbol{m}_{l\to \mathrm{H}} = \boldsymbol{0}$ on the cell edges $\boldsymbol{\gamma}_Y \subset Y_{\mathrm{N}}$, so there is $\langle \boldsymbol{h} \rangle_{\boldsymbol{\gamma}_Y} = \langle \boldsymbol{h} - \boldsymbol{m}_{l\to \mathrm{H}} \rangle_{\boldsymbol{\gamma}_Y} = \langle \boldsymbol{h} - \boldsymbol{m}_{l\to \mathrm{H}} \rangle_Y = \boldsymbol{H}$.

Let us now take stock of the status of the mathematical analysis of multiscale MQS nonlinear problem robust to emerging magnetization. First, it is to be shown that the two-scale problem robust to emerging magnetization can be defined as the limit of a problem sequence. This should probably be done using the methodology from [10,46,48] and/or the tools from [29] to deal with emerging magnetization, and those from [44,45] to deal with nonlinearity. Assuming that all the continuous and discrete problems used in (14) are shown to exist, the method introduces errors of two kinds that need to be considered. They are

(*i*) the modeling error, introduced by replacing the problem of interest with a limit two-scale problem, and
(*ii*) the discretization error, introduced by approximating the two-scale problem using a FE-HMM formulation.

A priori estimates of the convergence of the discretization error (*ii*) are shown in many analysis papers for linear scattering problems [31,48,50,52,54,56]. However, the authors are not aware of any estimation of (*ii*) for nonlinear MQS problems, nor of the modeling error (*i*) for MQS problems or scattering problems [10,53]. However, experimental validation that the modeling error converges was achieved, for example in [10] and in the present paper. For literature on (*ii*), see e.g. [57,58]. The need for modeling error estimate is particularly important here because the two-scale limit problem depends on the scaling assumptions made in the ϵ-sequence. So (*ii*) is needed not only to validate – a priori or a posteriori – that the method introduces limited error, but also in order to choose the best limit problem for a given real world problem. Especially if the actual physical parameters lie in between two regimes, for example low and high frequency.

In conclusion, the derivation of accurate two-scale formulations of Maxwell's equations that are robust to the emergence of additional magnetization is fairly well understood from the physical, mathematical and numerical point of view. However, the rigorous analysis for the definition of the continuous two-scale MQS problem and estimates of the associated errors in this context appear to be open problems.

4. Discrete FE-HMM formulation

This section introduces the two-scale B-conforming continuous formulations and their weak discretized form for the FE-HMM (or FE^2) implementation. The equations are mostly equivalent to those derived in [22–25,29], up to the choice of time discretization method and of boundary conditions in the cell.

Additionally, six methods for the upscaling of the magnetic field are introduced and compared. Algorithm 1 is employed to implement the FE-HMM. The indices n and K are the time step and macroscopic iteration index respectively. In our implementation, one cell problem is associated to each barycenter of an element of $\Omega_{\mathrm{H},h}$, denoted by $\boldsymbol{x}_B \in \mathcal{B}(\Omega_{\mathrm{H},h})$, and the upscaled quantities are constant per element.

4.1. Macroscopic equations

The weak discrete form of the macroscopic B-conforming problem at time step $n+1$ and macroscopic iteration $K+1$ is: find $\boldsymbol{A} \in \boldsymbol{H}_{h,\boldsymbol{0}_\tau,\boldsymbol{0}_{\Gamma_b}}(\mathbf{curl}; \Omega_h)$ s.t.

$$\int_{\Omega_{\mathrm{M},h}} \frac{1}{\mu_0} \mathbf{curl}\, \boldsymbol{A} \cdot \mathbf{curl}\, \boldsymbol{A}' + \int_{\Omega_{\mathrm{H},h}} \left(\boldsymbol{H}^{n+1,K} + \frac{\partial \boldsymbol{H}}{\partial \boldsymbol{B}}^{n+1,K} \cdot \mathbf{curl}\left(\boldsymbol{A} - \boldsymbol{A}^{n+1,K} \right) \right) \cdot \mathbf{curl}\, \boldsymbol{A}' = \int_{\Omega_{\mathrm{s},h}} \boldsymbol{J}_{\mathrm{s}} \cdot \boldsymbol{A}' \tag{17}$$

[8] The periodized 3D cell is the torus $\mathbb{T}^3$, these classes are the representatives of the first homology group $\mathbb{T}^3$ that is of dimension three.

Algorithm 1 FE-HMM algorithm for a transient B-conforming problem

Set initial conditions at $t_{n=0} = 0$
for t_{n+1} in $(0, T_f]$ **do** ▷ Time step may be adaptive
  Initialize macro solution (at $K = 0$)
  do macro iteration $K + 1$ ▷ Macro NL Loop, iterations may be relaxed
    for $\boldsymbol{x}_B$ in $\mathcal{B}(\Omega_{\mathrm{H},h})$ **do** ▷ Cell resolutions, can be fully parallelized
      Downscale $\boldsymbol{B}^{n+1,K}(\boldsymbol{x}_B)$, initialize cell solutions (at $k = 0$)
      for each cell iteration $k + 1$ **do** ▷ Only involves several iterations for NL fine-scale magnetic law
        Solve cell FEM problem at $\boldsymbol{x}_B$ (22)
      Upscale $\boldsymbol{H}^{n+1,K+1}(\boldsymbol{x}_B)$,
    → repeat to compute $\frac{\partial \boldsymbol{H}}{\partial \boldsymbol{B}}^{n+1,K+1}(\boldsymbol{x}_B)$
  Solve macro FEM problem to have $\boldsymbol{A}^{n+1,K+1}$, $\boldsymbol{B}^{n+1,K+1}$ (17)
  while Macro problem converged (or diverged)
  Upscale E.C. losses density $\langle \boldsymbol{j}^n \cdot \boldsymbol{e}^n \rangle_{Y_h}$, compute $\mathcal{P}_{\mathrm{JL}}^{\mathrm{HMM}}(t_n) = \int_{\Omega_{\mathrm{H},h}} \langle \boldsymbol{j}^n \cdot \boldsymbol{e}^n \rangle_{Y_h}$ ▷ E.C. losses post-processing

for all $\boldsymbol{A}' \in \boldsymbol{H}_{h,\mathbf{0}_\Gamma,\mathbf{0}_{\Gamma_b}}(\mathbf{curl}; \Omega_h)$. $\boldsymbol{H}^{n+1,K}$ and $\frac{\partial \boldsymbol{H}}{\partial \boldsymbol{B}}^{n+1,K}$ are upscaled from each cell per $\boldsymbol{x}_B \in \mathcal{B}(\Omega_{\mathrm{H},h})$, using the source $\boldsymbol{B}^{n+1,K} = \mathbf{curl}\, \boldsymbol{A}^{n+1,K}$ at $\boldsymbol{x}_B$, which is the magnetic induction from the previous iteration. These upscaled quantities implicitly depend on the previous cell solutions $\boldsymbol{a}^n$, enabling transient and hysteretic effect. Using relaxation by a factor ω, the solution at the next iteration is $\boldsymbol{A}^{n+1,K+1} = \omega \boldsymbol{A} + (1-\omega)\boldsymbol{A}^{n+1,K}$.

The incremental reluctivity tensor $\frac{\partial \boldsymbol{H}}{\partial \boldsymbol{B}}$ is computed using a finite difference method. In 3D, this requires three additional resolutions of the cell problem, with sources $\boldsymbol{B} + \eta \boldsymbol{e}_j$ for $j = \{x, y, z\}$. The resolutions are independent and can be solved in parallel, they require iterations for nonlinear cell problems. The tensor is then computed as follows

$$\frac{\partial \boldsymbol{H}}{\partial \boldsymbol{B}}(t, \boldsymbol{B}) = \left(\frac{\partial H_i}{\partial B_j}(t, \boldsymbol{B}) \right)_{i,j} \approx \eta^{-1} \left(\left(\boldsymbol{H}(t, \boldsymbol{B} + \eta \boldsymbol{e}_j) - \boldsymbol{H}(t, \boldsymbol{B}) \right) \cdot \boldsymbol{e}_i \right)_{i,j}. \tag{18}$$

4.2. Cell problems

A cell problem at $\boldsymbol{x} \in \Omega_{\mathrm{H}}$ features an unknown magnetic vector potential $\boldsymbol{a}(\boldsymbol{x}, \boldsymbol{y})$ defined by

$$\boldsymbol{a}(\boldsymbol{x}, \boldsymbol{y}) = \boldsymbol{A}(\boldsymbol{x}) + \boldsymbol{a}_{\mathrm{c}}(\boldsymbol{x}, \boldsymbol{y}) + \frac{1}{2} \mathbf{curl}_{\boldsymbol{x}} \left(\boldsymbol{A}(\boldsymbol{x}) \right) \times \boldsymbol{y} \quad \text{for } \boldsymbol{y} \in Y, \tag{19}$$

with $\boldsymbol{a}_{\mathrm{c}} \in \boldsymbol{H}^{\#}_{\mathbf{0}_{Y}}(\mathbf{curl}; Y)$. This function space is defined by

$$\boldsymbol{H}^{\#}_{\mathbf{0}_{Y}}(\mathbf{curl}; Y) = \left\{ \boldsymbol{a}_{\mathrm{c}} \in \boldsymbol{H}^{\#}(\mathbf{curl}; Y) \;\middle|\; \boldsymbol{a}_{\mathrm{c}} \cdot \boldsymbol{t}\big|_{\gamma_Y} = 0 \right\}, \tag{20}$$

meaning $\boldsymbol{a}_{\mathrm{c}}$ is Y-periodic and has zero tangential trace to the edges of the cell. The latter condition ensures that $\langle \boldsymbol{a}(\boldsymbol{x}, \boldsymbol{y}) \rangle_{\gamma_Y} = \boldsymbol{A}(\boldsymbol{x})$, by fixing the part of the kernel of $\mathbf{curl}_{\boldsymbol{y}}$ that is due to the periodicity.[9]

The purpose of the splitting (19) is threefold: fixing $\langle \boldsymbol{a} \rangle_Y$, being able to use a periodic unknown field in Y, and imposing the source $\langle \mathbf{curl}_{\boldsymbol{y}}\, \boldsymbol{a} \rangle_Y = \boldsymbol{B}$. Indeed, the Y-curl of $\boldsymbol{a}$ in (19) is $\mathbf{curl}_{\boldsymbol{y}}\, \boldsymbol{a} = \mathbf{curl}_{\boldsymbol{x}} \boldsymbol{A}(\boldsymbol{x}) + \mathbf{curl}_{\boldsymbol{y}}\, \boldsymbol{a}_{\mathrm{c}}(\boldsymbol{y})$ where $\mathbf{curl}_{\boldsymbol{x}} \boldsymbol{A}(\boldsymbol{x})$ is homogeneous in Y equal to $\boldsymbol{B}(\boldsymbol{x})$. Also, $\boldsymbol{A}(\boldsymbol{x})$ has no particular meaning, it is arbitrarily fixed to $\boldsymbol{A}(\boldsymbol{x}) = \mathbf{0}$ at all time, see also [29, Eq. (45)] or [30, p. 97].

Plugging (19) into the B-conforming formulation leads to the following strong formulation of the cell problem

$$\mathbf{curl}_{\boldsymbol{y}} \left(\nu \cdot (\boldsymbol{B} + \mathbf{curl}_{\boldsymbol{y}}\, \boldsymbol{a}_{\mathrm{c}}(\boldsymbol{y})) \right) + \sigma \left(\partial_t \boldsymbol{a}_{\mathrm{c}}(\boldsymbol{y}) + \frac{1}{2} \partial_t \boldsymbol{B} \times \boldsymbol{y} \right) = \mathbf{0} \quad \forall \boldsymbol{y} \in Y(\boldsymbol{x}). \tag{21}$$

A weak spatially discrete problem is derived from (21) using a Coulomb gauge weakly imposed by a periodic scalar potential [36]. It reads find $\boldsymbol{a}_{\mathrm{c}} \in \boldsymbol{H}^{\#}_{h,\mathbf{0}_{\boldsymbol{\gamma}_Y}}(\mathbf{curl}; Y)$, $\xi_{\mathrm{p}} \in \boldsymbol{H}^{\#}_{h}(\mathbf{grad}; Y_{\mathrm{N}})$ such that

$$\begin{aligned} &\int_{Y_h} \boldsymbol{\nu} \cdot (\boldsymbol{B} + \mathbf{curl}\, \boldsymbol{a}_{\mathrm{c}}) \cdot \mathbf{curl}\, \boldsymbol{a}_{\mathrm{c}}{}' + \int_{Y_{\mathrm{C},h}} \sigma \left(\partial_t \boldsymbol{a}_{\mathrm{c}} + \frac{1}{2} \partial_t \boldsymbol{B} \times \boldsymbol{y} \right) \cdot \boldsymbol{a}_{\mathrm{c}}{}' + \int_{Y_{\mathrm{N},h}} \lambda_1 \mathbf{grad}\, \xi_{\mathrm{p}} \cdot \boldsymbol{a}_{\mathrm{c}}{}' = 0, \\ &\int_{Y_{\mathrm{N},h}} \lambda_1 \boldsymbol{a}_{\mathrm{c}} \cdot \mathbf{grad}\, \xi_{\mathrm{p}}{}' + \lambda_2 \xi_{\mathrm{p}} \xi_{\mathrm{p}}{}' = 0, \end{aligned} \tag{22}$$

for all $\boldsymbol{a}_{\mathrm{c}}{}' \in \boldsymbol{H}^{\#}_{h,\mathbf{0}_{\boldsymbol{\gamma}_Y}}(\mathbf{curl}; Y)$, $\xi_{\mathrm{p}}{}' \in \boldsymbol{H}^{\#}_{h}(\mathbf{grad}; Y_{\mathrm{N}})$, where $\partial_t \boldsymbol{B} = \frac{1}{\Delta t}(\boldsymbol{B} - \boldsymbol{B}^n)$ and $\lambda_1 > 0$ and $\lambda_2 \geq 0$ are Lagrange multiplier parameters. The Coulomb gauge is used here to avoid implementing a Y-periodic tree required for the tree gauge, although such tree can be built [25].

[9] The constraint $\boldsymbol{a}_{\mathrm{c}} \cdot \boldsymbol{t}\big|_{\gamma_Y} = 0$ is stronger than the required $\langle \boldsymbol{a}_{\mathrm{c}} \rangle_{\gamma_Y} = \mathbf{0}$, but the latter is less straightforward to implement.

Table 1
Summary of the upscaling methods for $\boldsymbol{H}$ discussed in the paper, with their advantages and drawbacks. Apart from the volume average $\langle \boldsymbol{h} \rangle_Y$ that is not always correct, all methods are mathematically equivalent in the continuous setting for periodic cell fulfilling the insulation assumption (1), except possibly the last method (25) in the very unlikely presence of dominant magnetic quadrupoles. $\langle \boldsymbol{h} - \boldsymbol{h}_c \rangle_Y$ is the most generalizable method for periodic cells with weaker assumptions than (1), and Wulfinghoff's average is the most general method as it can be applied to non-periodic representative volume element.

Method name	Symbol	Eq., [Reference]	Advantages	Drawbacks
Volume average	$\langle \boldsymbol{h} \rangle_Y$	(23)	Simple implementation, general to any cell geometry	Limited to magnetostatic or when $\boldsymbol{M}_{l\to\mathrm{H}}$ is negligible
Edge average	$\langle \boldsymbol{h} \rangle_{\gamma_Y}$	(15), [27, Eq. (5)]	General to any solution	Numerical accuracy might be limited [28]
Tangential boundary average	$\langle \boldsymbol{h} \rangle_{\partial Y_\parallel}$	(24), [28, Eq. (2)]	Surface integration (numerically more accurate than path)	Limited to domains such that $Y_C \cap \partial Y = \emptyset$
Periodic correction volume average	$\langle \boldsymbol{h} - \boldsymbol{h}_c \rangle_Y$	(27), [new]	Volume integration, may be generalized to any cell	Cost of the FEM projection for $\boldsymbol{h}_c$
Magnetization volume average	$\langle \boldsymbol{h} - \boldsymbol{m}_{l\to\mathrm{H}} \rangle_Y$	(26), [24, Eq. (8)]	Like $\langle \boldsymbol{h} - \boldsymbol{h}_c \rangle_Y$, but cheaper if Y_C is smaller than Y	Cost of the FEM projection for $\boldsymbol{m}_{l\to\mathrm{H}}$
Wulfinghoff's boundary average	$\int_{\partial Y} \frac{\boldsymbol{y}}{2\lvert Y\rvert} \times (\boldsymbol{h} \times \boldsymbol{n}) \,\mathrm{d}S$	(25), [29, Eq. (20)]	Surface integration, general to any cell geometry	Possibly not robust to quadrupole magnetization

4.3. Numerical method for the upscaling of the magnetic field

Let us now introduce six numerical methods for the upscaling of the magnetic field and incremental reluctivity from periodic cell problems. The classical one is the volume average $\langle \boldsymbol{h} \rangle_Y$. In the solutions of (22), $\boldsymbol{h}$ is given by $\boldsymbol{\nu}(\boldsymbol{b})\cdot(\boldsymbol{b})$ where $\boldsymbol{b} = \boldsymbol{B} + \mathbf{curl}\,\boldsymbol{a}_c$, leading to

$$\boldsymbol{H} = \langle\, \boldsymbol{\nu}(\boldsymbol{B} + \mathbf{curl}\,\boldsymbol{a}_c) \cdot (\boldsymbol{B} + \mathbf{curl}\,\boldsymbol{a}_c) \,\rangle_Y . \tag{23}$$

This method is certainly accurate for magnetostatic cell problems for which $\mathbf{curl}\,\boldsymbol{h} = \boldsymbol{0}$ in the whole cell, because $\boldsymbol{m}_{l\to\mathrm{H}}$ vanishes (12). Also, the inequality derived in [26, Sec. 3.2] shows that $(\boldsymbol{H} - \langle \boldsymbol{h} \rangle_Y) \cdot \partial_t \boldsymbol{B} = -\boldsymbol{M}_{l\to\mathrm{H}} \cdot \partial_t \boldsymbol{B}$ becomes negligible when the electric power in the cell becomes negligible in the total electromagnetic power. Given that the dynamic magnetization $\boldsymbol{m}_{l\to\mathrm{H}}$ should align with $\partial_t \boldsymbol{B}$,[10] this criterion gives a likely sufficient condition to use the volume average.

Otherwise, one of the next methods shall be used, they should be robust to significant $\boldsymbol{M}_{l\to\mathrm{H}}$. The first possible method is to use the edge average (15), implemented as $\langle \boldsymbol{\nu}(\boldsymbol{B} + \mathbf{curl}\,\boldsymbol{a}_c) \cdot (\boldsymbol{B} + \mathbf{curl}\,\boldsymbol{a}_c) \rangle_{\gamma_Y}$. Numerically, it requires computing the tangential trace of $\boldsymbol{h}$ to the edges of the cell. Depending on the software used, this may require using a projection of $\boldsymbol{\nu}\cdot\mathbf{curl}\,\boldsymbol{a}_c$ onto $\boldsymbol{H}^{\#}_h(\mathbf{curl};)$ in the elements adjacent to the cell edges, more details are given after Eq. (2.79) in [30, p. 103].

The edge average method uses a thin support for integration that may result in reduced accuracy and stability. To circumvent this issue, averages on the boundary can be used. The tangential boundary average $\langle\ \rangle_{\partial Y_\parallel}$ is defined by:

$$\langle \boldsymbol{h} \rangle_{\partial Y_\parallel} := \begin{bmatrix} \frac{1}{2(k_x k_y + k_x k_z)} & 0 & 0 \\ 0 & \frac{1}{2(k_y k_x + k_y k_z)} & 0 \\ 0 & 0 & \frac{1}{2(k_z k_x + k_z k_y)} \end{bmatrix} \cdot \int_{\partial Y} \boldsymbol{h}_{\boldsymbol{t}} \,\mathrm{d}S, \qquad \text{with} \qquad \boldsymbol{h}_{\boldsymbol{t}} = (\boldsymbol{n} \times \boldsymbol{h}) \times \boldsymbol{n}, \tag{24}$$

where each component $H_i = \boldsymbol{e}_i \cdot \langle \boldsymbol{h} \rangle_{\partial Y_\parallel}$ is normalized by the surface of the four faces of Y to which the component is tangent. This average equals the edge average when $\boldsymbol{h}$ is Y-periodic and $\boldsymbol{n} \cdot \mathbf{curl}\,\boldsymbol{h}\big|_{\partial Y} = 0$. This formula was first proposed by [28], and also used in [24,25]. Similarly to the edge average, it might be necessary to project $\boldsymbol{\nu}\,\mathbf{curl}\,\boldsymbol{a}_c$ onto $\boldsymbol{H}^{\#}_h(\mathbf{curl};)$ in the elements adjacent to ∂Y in order to compute the tangential component $\boldsymbol{h}_{\boldsymbol{t}}$, see discussion after Eq. (2.82) in [30, p. 104].

Another method using a different boundary average has recently been proposed in [29, Eq. (20)],

$$\boldsymbol{H} = \frac{1}{|Y|} \int_{\partial Y} \frac{1}{2}\, \boldsymbol{y} \times (\boldsymbol{h} \times \boldsymbol{n}) \,\mathrm{d}S = \langle \boldsymbol{h} \rangle_Y - \frac{1}{|Y|} \int_Y \frac{1}{2}\, \boldsymbol{y} \times \mathbf{curl}\,\boldsymbol{h} \,. \tag{25}$$

This formula features the subtraction of the magnetization dipole moment (average of $1/2\,\boldsymbol{y} \times \boldsymbol{j}$) from the volume average $\langle \boldsymbol{h} \rangle_Y$. So it is not mathematically equivalent to $\langle \boldsymbol{h} \rangle_{\gamma_Y}$ and $\langle \boldsymbol{h} \rangle_{\partial Y_\parallel}$ as it would fail to filter out quadripole – or higher order – magnetization moments. However, having such magnetization moment seems to be rare in general, and the derivation of [29] suggests that this edge case will not happen in practice if the source term for the magnetic vector potential is only "first order in $\boldsymbol{y}$" as in (19). Unfortunately, this article appeared after the numerical experiments of this paper were finished, so no numerical comparison was made for the present article.

[10] This can be seen from the vector product in $\mathbf{curl}\,\boldsymbol{m}_{l\to\mathrm{H}} = \sigma(\partial_t \boldsymbol{a}_c + 1/2\,\partial_t \boldsymbol{B} \times \boldsymbol{y})$.

Table 2
Main parameters for the accuracy study cases.

Study case	f (MHz)	μ (Hm^{-1})	σ (MSm^{-1})	δ (μm)	diam(Y_C)	T_f (periods)
nonlinear	0.3	(28) with $\mu_r^{\max} = 100$, $B_s = 1.5$ T	10.0	$29.1 \leq \delta \leq 291$	80 μm	1.25
linear	10	μ_0	$5.97e^1$	21	90 μm	2.25

Alternatively, the dynamic magnetization $\boldsymbol{m}_{l\to\mathrm{H}}$ defined in (12) can be numerically computed in $\boldsymbol{H}_{\boldsymbol{0}}(\mathbf{curl}; Y_C)$ using the formulation

$$\mathbf{curl}\,\mathbf{curl}\,\boldsymbol{m}_{l\to\mathrm{H}} = \mathbf{curl}\left(\sigma\partial_t\left(\boldsymbol{a}_c + \frac{1}{2}\boldsymbol{B}\times\boldsymbol{y}\right)\right) \quad \text{in } Y_C. \tag{26}$$

The expression under the **curl** in the right-hand-side of (26) is the confined current term from (21). After solving for (26), $\boldsymbol{m}_{l\to\mathrm{H}}$ can be used to upscale the magnetic field using $\boldsymbol{H} = \langle \boldsymbol{h} - \boldsymbol{m}_{l\to\mathrm{H}} \rangle_Y$. A discrete weak form of (26) is given in Appendix A.4. Thanks to the boundary condition of $\boldsymbol{m}_{l\to\mathrm{H}}$, the choice of gauge for the kernel of the **curl** operator do not impact $\langle \boldsymbol{m}_{l\to\mathrm{H}} \rangle_Y$, this is shown in [30, p. 107]. This formulation was first introduced in 2D in [24].

Finally, let us introduce a new method, inspired by the discretization of the H-conforming formulation of the cell problem. In this formulation, the magnetic field is discretized as $\boldsymbol{h}(\boldsymbol{y}) = \boldsymbol{H}(\boldsymbol{x}) + \boldsymbol{h}_c(\boldsymbol{y})$ where $\langle \boldsymbol{h}_c \rangle_{\boldsymbol{\gamma}_Y} = \boldsymbol{0}$.[11] Applying the volume average and re-arranging leads to $\boldsymbol{H} = \langle \boldsymbol{h} - \boldsymbol{h}_c \rangle_Y$. This correction field may be approximated by $\widetilde{\boldsymbol{h}}_c \in \boldsymbol{H}^{\#}_{\boldsymbol{0}\boldsymbol{\gamma}_Y}(\mathbf{curl}; Y)$ using the projection

$$\mathbf{curl}\,\mathbf{curl}\,\widetilde{\boldsymbol{h}}_c = \mathbf{curl}\left(\sigma\partial_t\left(\boldsymbol{a}_c + \frac{1}{2}\boldsymbol{B}\times\boldsymbol{y}\right)\right) \quad \text{in } Y. \tag{27}$$

The difference with (26) is that this formulation is written in the whole cell, not only Y_C, so it may be more expensive and have slightly different numerical behavior. A discrete weak form of (27) is given in Appendix A.5. Similarly to (26), the gauge choice does not impact the result.

All introduced upscaling methods are summarized in Table 1, the first five will be used and compared in the following simulations.

5. Numerical experiments

For the numerical experiments, two sets of material laws for the active (conducting) part of the heterogeneous domain will be used, they are summarized in Table 2. The first set features a nonlinear magnetic law to study the capability of the method to solve 3D transient NL problems and the numerical stability of the different upscaling methods. The second set features a linear law and will lead to high cell magnetization, in order to validate the accuracy of the different $\boldsymbol{H}$ upscaling definitions.

The NL magnetic law μ_{FK} is the analytic Fröhlich–Kennelly law [59], defined by the permeability

$$\mu_{\mathrm{FK}}(\boldsymbol{h}) = \mu_0 + \frac{(\mu_r^{\max} - 1)B_s}{(\mu_r^{\max} - 1)\|\boldsymbol{h}\| + B_s/\mu_0} \tag{28}$$

where B_s is the saturation induction and $\mu_r^{\max}$ is the maximum relative permeability. It can be verified that $\boldsymbol{h} \to \boldsymbol{b}(\boldsymbol{h})$ is equivalent to $\mu_0\mu_r^{\max}\boldsymbol{h}$ near $\|\boldsymbol{h}\| = 0$, and to $\mu_0\boldsymbol{h}$ when $\mu_0\|\boldsymbol{h}\| \gg B_s$. The inverse law $\boldsymbol{b} \to \boldsymbol{h}(\boldsymbol{b})$, used in the B-conforming formulation, is given in Appendix A.1.

Geometry of the reference problem

A cubic heterogeneous domain (the "core") Ω_l of width 0.8 mm and centered at the origin is considered. It consists of $8 \times 8 \times 8$ cubic cells of width 100 μm, each containing a conducting ball Y_C of diameter diam(Y_C) = 80 μm or 90 μm, inside an insulator matrix Y_N. The insulator has zero conductivity and permeability μ_0. The core is surrounded by air and a toroidal coil Ω_s fed by a prescribed idealized current source. The coil has an outer radius of 3 mm and a cross-section diameter of 200 μm. The modeling domain is restricted to a spherical box of diameter 6 cm. Three symmetry planes of the geometry are exploited in order to only simulate one eighth of Ω, that is 64 cells of Ω_l, as shown in Fig. 4.

The reference formulation is (6). The current source imposed in Ω_s is

$$\boldsymbol{j}_s(\boldsymbol{x}, t) = \frac{I(t)}{A_C}\left(-\sin(\theta(\boldsymbol{x}))\,\boldsymbol{e}_x + \cos(\theta(\boldsymbol{x}))\,\boldsymbol{e}_y\right), \tag{29}$$

where $A_C = \pi 10^{-8}$ m^2 is the coil cross-section, $I(t) = 1000\sin(2\pi f t)$ A is the total current accounting for all turns of the coil, f is the source frequency and $\theta(x, y, z) = \mathrm{atan}(y/x)$ the angle of the direction of the coil. This source is analytically divergence free, no correction method ensuring the null divergence (such techniques are summarized in [36]) was needed here. The simulations start with null initial conditions $\boldsymbol{a}(t = 0) = \boldsymbol{0}$ and $v(t = 0) = 0$ everywhere.

The reference is solved on a personal computer, using the direct LU solver provided by MUMPS, multi-threaded on 10–15 threads. To grasp the complexity trend of solving this problem, Table 3 shows the number of tetrahedra meshing the heterogeneous domain Ω_l and the time to solve the linear system of the problem for one NL iteration as a function of the number n of spatial periods in one direction. The cost is unaffordable for $n > 10$.

[11] The exact discretization is $\boldsymbol{h}(\boldsymbol{x}, \boldsymbol{y}) = \boldsymbol{H}(\boldsymbol{x}) + \mathbf{grad}\,\phi_p(\boldsymbol{y})|_{Y_N} + \boldsymbol{h}_C(\boldsymbol{y})|_{Y_C}$ with $\phi_p \in H_0(\mathbf{grad}; Y_N)$, $\boldsymbol{h}_C \in \boldsymbol{H}(\mathbf{curl}; Y_C)$ and $[\![(\mathbf{grad}\,\phi_p - \boldsymbol{h}_C) \times \boldsymbol{n}]\!]|_{\Gamma_{C\backslash N}} = 0$. But due to the insulation of the cell, one can show that $\langle \mathbf{grad}\,\phi_p|_{Y_N} + \boldsymbol{h}_C|_{Y_C} \rangle_{\boldsymbol{\gamma}_Y} = \langle \mathbf{grad}\,\phi_p|_{Y_N} \rangle_{\boldsymbol{\gamma}_Y} = \boldsymbol{0}$, so $\boldsymbol{h} - \boldsymbol{H}$ can be fairly well approximated by a $\widetilde{\boldsymbol{h}}_c \in \boldsymbol{H}^{\#}_{\boldsymbol{0}\boldsymbol{\gamma}_Y}(\mathbf{curl}; Y)$.

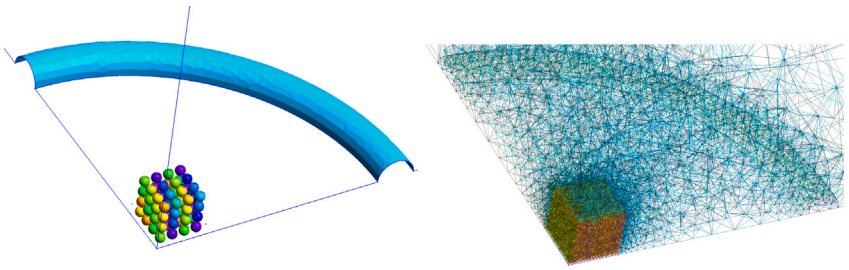

Fig. 4. Reference geometry (left) and mesh (right) of the heterogeneous periodic magnetic material surrounded by a coil used in the numerical tests.

Table 3
Resolution cost trend of the reference (non-homogenized) problem (using naive extrapolation for $n > 10$). This cost grows cubically with either the number of elements or of degrees-of-freedom (linear system resolution cost). In 3D, it thus grows like $n^{3\times3} = n^9$, where n is proportional to the inverse diameter of the heterogeneities.

n	1	3	6	10	100	1000
Ω_c tetrahedra	3.6k	98k	778k	3.6M	3.6G	3.6T
One system solve	4 s	96 s	10 m	35 m	>7 d	≫13 y

Quantities of interest

Two global quantities are monitored to study the accuracy of the solutions, the eddy current (EC) losses $\mathcal{P}_{\text{JL}}$ and electromagnetic power $\mathcal{P}_{\text{em}}$ in the heterogeneous domain Ω_l or its homogenized counterpart Ω_{H}. The EC losses are computed as

$$\mathcal{P}_{\text{JL}}^{\text{ref}}(t) = \int_{\Omega_{l,h}} \boldsymbol{j}(t)\cdot\boldsymbol{e}(t) \quad \text{and} \quad \mathcal{P}_{\text{JL}}^{\text{HMM}}(t) = \int_{\Omega_{\text{H},h}} \langle \boldsymbol{j}(t)\cdot\boldsymbol{e}(t)\rangle_{Y_h}, \tag{30}$$

and the powers are computed using

$$\mathcal{P}_{\text{em}}^{\text{ref}}(t) = \int_{\Omega_{l,h}} \boldsymbol{h}(t)\cdot\partial_t\boldsymbol{b}(t) + \boldsymbol{j}(t)\cdot\boldsymbol{e}(t) \quad \text{and} \quad \mathcal{P}_{\text{em}}^{\text{HMM}}(t) = \int_{\Omega_{\text{H},h}} \boldsymbol{H}(t)\cdot\partial_t\boldsymbol{B}(t). \tag{31}$$

The total power $\mathcal{P}_{\text{em}}^{\text{HMM}}$ contains no electric term since Ω_{H} is nonconducting. But the quantity should still contain the EC losses, provided that the dynamic magnetization is properly accounted for by correct upscaling methods. The metric used to compare these couples of instantaneous quantities (reference and homogenized) over a time interval $[0,T]$ is the following

$$L^2_{\text{Err}}(s^{\text{ref}}, s^{\text{HMM}}) = 100\sqrt{\frac{\int_{[0,T]}(s^{\text{ref}}(t) - s^{\text{HMM}}(t))^2\,dt}{\int_{[0,T]} s^{\text{ref}}(t)^2\,dt}}, \tag{32}$$

it is a percentage of $L^2([0,T])$ norm error.

Accuracy for nonlinear magnetic law

Our first experiment validates the capability of our method to tackle the difficult simulation of a 3D magnetic core simulation featuring nonlinearity, eddy currents with skin effect and magnetic saturation, in transient regime. A reference featuring a relatively small number geometric periods (64 meshed) is used, as the reference problem would otherwise not be solvable. Consequently, these accuracy experiments do not demonstrate computational advantage of HMM over the reference.

The skin depth δ varies between 29.1 μm and 291 μm depending on the saturation of the magnetic law, to compare with the ball radius that is 40 μm. The mesh for the macroscopic resolution has 29k elements and the cell meshes have 19k elements. The simulation runs for 4.16 μs (1.25 periods) at minimum 160 time steps (TS) per period, but the time step can be refined via adaptive time stepping. The time step is decreased if a multiscale iterative loop diverges, and extended when the same loop takes less than 3 iterations to converge.

A relaxation factor search is also used to help with the multiscale convergence. The factors $\omega = 1$, 0.75, 0.5, 0.25 and 0.005 are successively tested, and the first one yielding a macroscopic residual decrease is chosen. This relaxation factor research is quite costly because it requires computing the cell problems and upscaling their solutions to compute a new macroscopic residual. However, the numerical convergence of our implementation is not yet well controlled and understood. The fine-tuning of the hyper-parameters of the algorithm is challenging because they are numerous – e.g. the mesh sizes and iteration stopping criteria parameters for all macro and cell problems and the finite difference perturbation to compute the $\frac{\partial \boldsymbol{H}}{\partial \boldsymbol{B}}$ Jacobians – so identifying the critical ones is not straightforward. Convergence issues were encountered, they are visible in the presented results for certain methods. However, the presented results still show the correct multiscale modeling of magnetodynamic phenomena and accuracy of the method when it

Table 4
Summary of the convergence and performance of HMM obtained on magnetically nonlinear problems for the different $\boldsymbol{H}$ upscaling methods. Unstable methods did not reach the expected final time $T_f = 4.17$ µs, $\langle \boldsymbol{h} \rangle_{\boldsymbol{\gamma}_Y}$ because of a crash and $\langle \boldsymbol{h} \rangle_Y$ and $\langle \boldsymbol{h} - \boldsymbol{h}_c \rangle_Y$ due to exhaustion of the allocated computation time ("wall time"= 48 h). The "TS" column contains the total number of adaptive time steps performed. Comparing wall time on the same hardware shows that convergence difficulties lead to longer average runtime per time-step ($\langle \boldsymbol{h} \rangle_{\partial Y_\parallel}$ versus $\langle \boldsymbol{h} \rangle_Y$, or $\langle \boldsymbol{h} - \boldsymbol{m}_{\mathrm{I}\to\mathrm{H}} \rangle_Y$ versus $\langle \boldsymbol{h} - \boldsymbol{h}_c \rangle_Y$). The reference is competitive with HMM due to the low number of reference geometric period (64 meshed), and the cost of the HMM iterations associated to the macro-cell coupling, whereas the reference problem is monolithic.

Method	Hardware (# cores)	T_f (µs)	TS	Wall time (hours)
Reference	PC	4.17	200	55
HMM $\langle \boldsymbol{h} \rangle_{\partial Y_\parallel}$	GRICAD (48)	4.17	200	40
HMM $\langle \boldsymbol{h} \rangle_Y$	GRICAD (48)	1.15	99	48
HMM $\langle \boldsymbol{h} \rangle_{\gamma_Y}$	GRICAD (48)	0.19	31	8
HMM $\langle \boldsymbol{h} - \boldsymbol{m}_{\mathrm{I}\to\mathrm{H}} \rangle_Y$	Nic5 (32)	4.17	200	21
HMM $\langle \boldsymbol{h} - \boldsymbol{h}_c \rangle_Y$	Nic5 (32)	2.47	212	48

Table 5
Time integrated percentage of error (def. in (32)) for EC losses and $\mathcal{P}_{\mathrm{em}}$ predicted by HMM, for the nonlinear test case.

Nonlinear, $\mathcal{P}_{\mathrm{JL}}$		
Upscale method	$\langle \boldsymbol{h} \rangle_{\partial Y_\parallel}$	$\langle \boldsymbol{h} - \boldsymbol{m}_{\mathrm{I}\to\mathrm{H}} \rangle_Y$
L^2_{Err} (%)	0.23	0.88

Nonlinear, $\mathcal{P}_{\mathrm{em}}$		
Upscale method	$\langle \boldsymbol{h} \rangle_{\partial Y_\parallel}$	$\langle \boldsymbol{h} - \boldsymbol{m}_{\mathrm{I}\to\mathrm{H}} \rangle_Y$
L^2_{Err} (%)	0.44	0.60

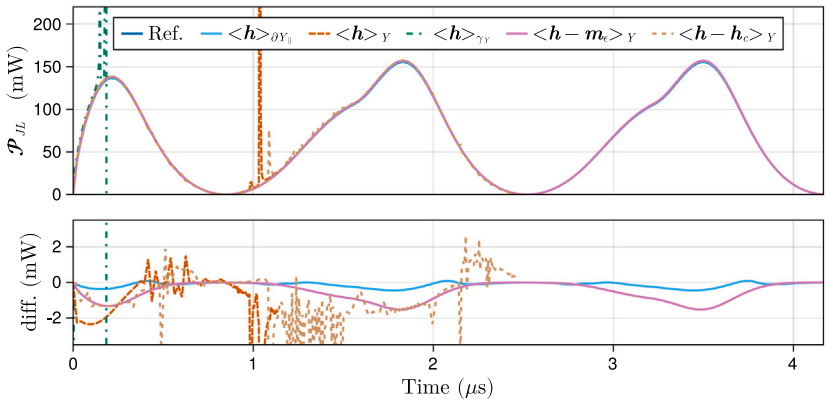

Fig. 5. Instantaneous total eddy current losses power (top) and associated relative error plot (bottom) for the accuracy test in nonlinear. The dynamic magnetization is negligible compared to $\boldsymbol{H}$, so all upscaling methods give correct result when they converge. However, convergence of the multiscale problem is not very stable and requires fine discretization parameters, and only the tangential boundary average $\langle \boldsymbol{h} \rangle_{\partial Y_\parallel}$ and average with cell magnetization $\langle \boldsymbol{h} - \boldsymbol{m}_{\mathrm{I}\to\mathrm{H}} \rangle_Y$ converged. The converging methods provide excellent accuracy.

converges. There clearly is room for improvement by carefully studying the impact of the parameters and trying different algorithms for the multiscale and nonlinear convergence and the $\frac{\partial \boldsymbol{H}}{\partial \boldsymbol{B}}$ upscaling, but that is out of the scope of this article.

The multiscale method is applied for five different upscaling methods, using two supercomputers, the GRICAD [60] from the Grenoble-Alpes University and Nic5 [61] of the University of Liège, some information of the runs are gathered in Table 4. The reference is solved on a personal computer (PC). Given that very different hardware were used, the computation times are not all comparable, we are mainly interested in accuracy and convergence. However, the runtimes show that convergence issues significantly impact the runtime due to increasing number of iterations. The estimation of the EC losses in the core are plotted in time in Fig. 5. The simulations that used the upscaling methods $\langle \boldsymbol{h} \rangle_{\partial Y_\parallel}$ and $\langle \boldsymbol{h} - \boldsymbol{m}_{\mathrm{I}\to\mathrm{H}} \rangle_Y$ converged, and their integrated percentage of error are given in Table 5. Excellent accuracy of approximately 1% of error is obtained for these converging methods. Also, B-H curves of the upscaled magnetic law are presented in Fig. 6 for two methods, they exhibit some magnetic nonlinearity, but it is not very visible due to the relatively low volume fraction of magnetic material in the cell of approximately 27%.

Accuracy for linear local magnetic law with dynamic hysteresis

For this experiment, the conductivity and diameter of the balls are increased to 59.7×10^6 S.m^{-1} and 90 µm respectively, and the frequency to 10 MHz. The skin depth is $\simeq$ 21 µm, smaller than the balls radius. The resolution runs for 2.25 periods, using 160 TS per period. No adaptive time stepping nor adaptive relaxation were needed there.

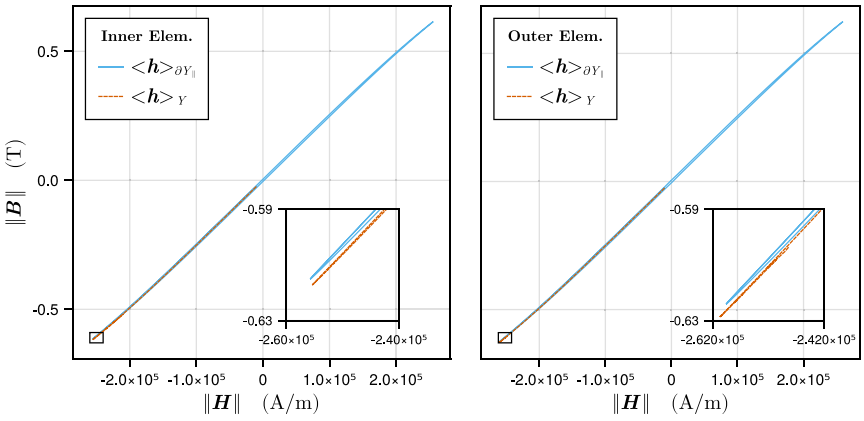

Fig. 6. $\boldsymbol{B}$-$\boldsymbol{H}$ curve (in norm) upscaled from the same cells as in figure Fig. 8, but for nonlinear fine-scale magnetic law. The dynamic magnetization is barely noticeable, and $\boldsymbol{H}$ and $\langle \boldsymbol{h} \rangle_Y$ upscale nearly the same law, but the latter did not complete a full period due to numerical instability.

Table 6
Time integrated percentage of error (def. in (32)) for EC losses and $\mathcal{P}_{\text{em}}$ predicted by HMM, for the linear test case.

Upscale method	$\langle \boldsymbol{h} \rangle_Y$	$\langle \boldsymbol{h} \rangle_{\partial Y_\parallel}$	$\langle \boldsymbol{h} \rangle_{\gamma_Y}$	$\langle \boldsymbol{h} - \boldsymbol{m}_{\mathfrak{h}\to\mathrm{H}} \rangle_Y$	$\langle \boldsymbol{h} - \boldsymbol{h}_c \rangle_Y$
$L^2_{\text{Err}}\mathcal{P}_{\text{JL}}$ (%)	31.1	0.67	0.97	1.13	0.48
$L^2_{\text{Err}}\mathcal{P}_{\text{em}}$ (%)	28.0	0.66	1.08	1.90	1.29

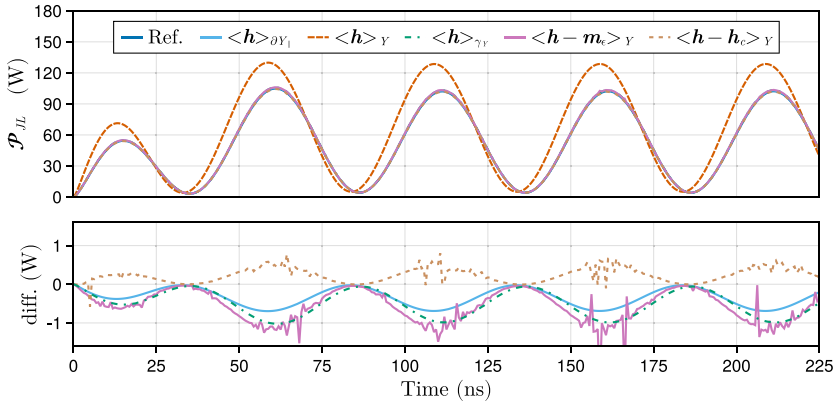

Fig. 7. Instantaneous total eddy current losses power (top) in the heterogeneous domain made of copper spheres and at 10 MHz, predicted by the reference method and the FE-HMM method with five different upscaling methods for $\boldsymbol{H}$. As expected, only the volume average $\langle \boldsymbol{h} \rangle_Y$ is completely wrong. The relative error plot (bottom) shows that all the other upscaling methods offer similar accuracy, although the methods with FEM projection $\langle \boldsymbol{h} - \boldsymbol{m}_{\mathfrak{h}\to\mathrm{H}} \rangle_Y$ and $\langle \boldsymbol{h} - \boldsymbol{h}_c \rangle_Y$ are less numerically stable.

The EC losses are plotted as a function of time in Fig. 7, and the integrated errors are given in Table 6. Unlike the nonlinear test case, all methods converge easily despite macroscopic iterations being required due to the emerging dynamic hysteresis. The solutions are completely wrong for the volume average upscaling. The error on EC losses is 28.0% when using the volume average, while it is below 1.90% using the others methods. The cut field maps in Fig. 10 qualitatively show agreement between the reference and homogenized local magnetic fields. The field maps shown in Fig. 9 illustrate how the eddy currents and dynamic magnetization create a phase shift between $\boldsymbol{H}$ and $\boldsymbol{B}$. This phase shift is also visible in the B-H curves of the upscaled law displayed in Fig. 8. Interestingly, the B-H curve for which $\boldsymbol{H}$ is defined as the volume average displays a constant slope. This is because the permeability is μ_0 everywhere and $\langle \nu_0 \boldsymbol{b} \rangle_Y = \nu_0 \langle \boldsymbol{b} \rangle_Y = \nu_0 \boldsymbol{B}$, so $\langle \boldsymbol{h} \rangle_Y = \nu_0 \boldsymbol{B}$ [27]. This upscaling cannot model the emergence of dynamic hysteresis.

Parametric study of the H upscaling method correctness

B-conforming multiscale formulations have been successfully applied using volume $\boldsymbol{H}$ upscaling in the literature, and the two previous experiments show that this may or may not be accurate. There is no general quantitative *a priori* criterion existing yet

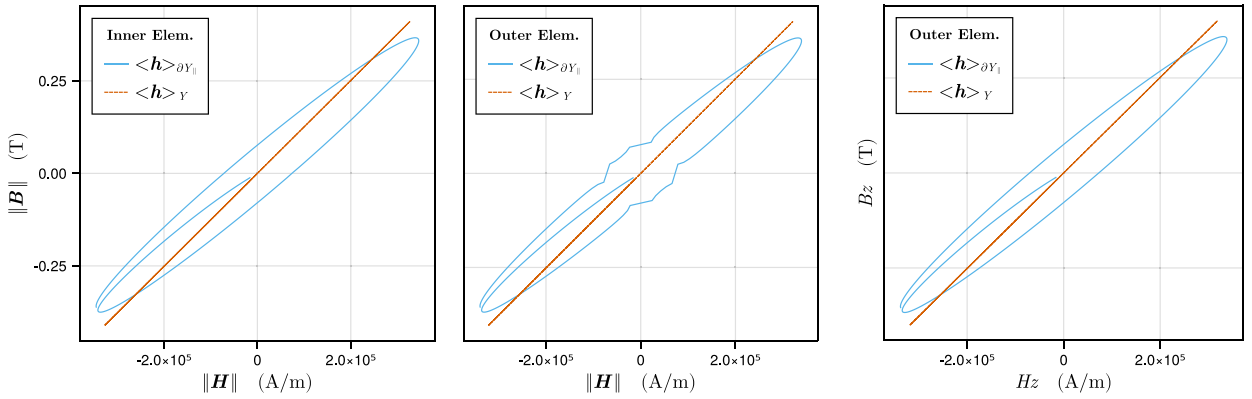

Fig. 8. $\boldsymbol{B}$-$\boldsymbol{H}$ curves (blue) and $\boldsymbol{B}$-$\langle \boldsymbol{h} \rangle_Y$ curves (orange) upscaled by the cell problem associated to the innermost cell of the core, at the intersection of the three symmetry planes, and the outer cell (center & left) of the core, its physical corner. Dynamic magnetization appears in the $\boldsymbol{B}$-$\boldsymbol{H}$ curve due to strong $\boldsymbol{m}_{l\to \mathrm{H}}$, but the $\boldsymbol{B}$-$\langle \boldsymbol{h} \rangle_Y$ law happens to be ν_0 as $\langle \boldsymbol{h} \rangle_Y = \langle \nu_0 \boldsymbol{b} \rangle_Y = \nu_0 \boldsymbol{B}$. This $\boldsymbol{B}$-$\boldsymbol{H}$ law could be modeled by a complex permeability tensor $\boldsymbol{\mu}$ in harmonic regime [14,17]. The non-smoothness of the curve (middle plot) is due to an out-of-phase rotation of $\boldsymbol{B}$ and $\boldsymbol{H}$, but the relation between each couple of components of $\boldsymbol{B}$ and $\boldsymbol{H}$ are smooth (e.g. B_z-H_z in the right plot). (For interpretation of the references to color in this figure legend, the reader is referred to the web version of this article.)

Table 7
Percentage of error on EC losses and electromagnetic power prediction by HMM using the meshes in Fig. 12, integrated over the whole simulation time. Excellent agreement with reference is reached before the multiscale convergence becomes unstable (for 125 macro elements).

Nonlinear $\mathcal{P}_{\mathrm{JL}}$					
N_{Mac}	1	8	27	64	125
L^2_{Err} (%)	6.09	1.79	0.32	0.26	2.26

Nonlinear $\mathcal{P}_{\mathrm{em}}$					
N_{Mac}	1	8	27	64	125
L^2_{Err} (%)	5.58	0.74	0.04	0.40	1.38

to predict when the cell dynamic magnetization impacts $\langle \boldsymbol{h} \rangle_Y$. Next, a parametric study of the interplay between electric power and the amount of dynamic magnetization in a single independent cell is conducted. The maximum magnetic permeability and frequency are varied. The cell geometry and physical properties are that of the nonlinear case. The quantity H_{err} is used to measure the discrepancy between $\boldsymbol{H}$ and $\langle \boldsymbol{h} \rangle_Y$ over one period:

$$H_{\mathrm{err}} = \frac{\int_{[0,T]} \|\boldsymbol{H}(t) - \langle \boldsymbol{h}(t) \rangle_Y\|^2 dt}{\int_{[0,T]} \|\boldsymbol{H}(t)\|^2 dt}, \tag{33}$$

it is a percentage of the difference between the $L^2([0,T])$ norm of the two quantities. It is compared with the square root of the electric power share in total power P_{rat} defined similarly by

$$P_{\mathrm{rat}} = \frac{\int_{[0,T]} \mathcal{P}_{\mathrm{JL}}{}^2 dt}{\int_{[0,T]} \mathcal{P}_{\mathrm{em}}{}^2 dt}, \quad \text{where} \quad \mathcal{P}_{\mathrm{JL}}(t) = \int_{Y_h} \boldsymbol{j}(t) \cdot \boldsymbol{e}(t), \quad \mathcal{P}_{\mathrm{em}}(t) = \int_{Y_h} \boldsymbol{h}(t) \cdot \partial_t \boldsymbol{b}(t) \; + \; \boldsymbol{j}(t) \cdot \boldsymbol{e}(t). \tag{34}$$

The results are shown in Fig. 11. $\boldsymbol{M}_{l\to \mathrm{H}}$ is only impactful at quite high frequency, over 10 MHz, and the maximum magnetic permeability is not very important due to the saturation of the material. Although not studied here, the most impactful parameter is the diameter of the conducting particle, because the EC losses – thus also $\boldsymbol{M}_{l\to \mathrm{H}}$ – are well known to be proportional to the surface area enclosed by the eddy current loops. The authors expect the discrepancy would appear at way lower frequency for say a 1 mm thick iron sheet.

Convergence of the discretization error

The following experiment is a convergence test with the refinement of the macroscopic mesh. The nonlinear test case is solved using meshes of the heterogeneous domain consisting of $N_{\mathrm{Mac}} = 1$, 8, 27, 64 and 125 elements respectively, see Fig. 12. The frequency is set to $f = 100$ kHz, and the intensity of the current source to $I = 800$ A. The boundary average upscaling $\langle h \rangle_{\partial Y_\parallel}$ is used.

The EC losses are plotted as a function of time in Fig. 13 and integrated errors are given in Table 7. The results demonstrate the convergence of the method with mesh refinement, until numerical instability of the multiscale convergence appears for the bigger mesh $N_{\mathrm{Mac}} = 125$.

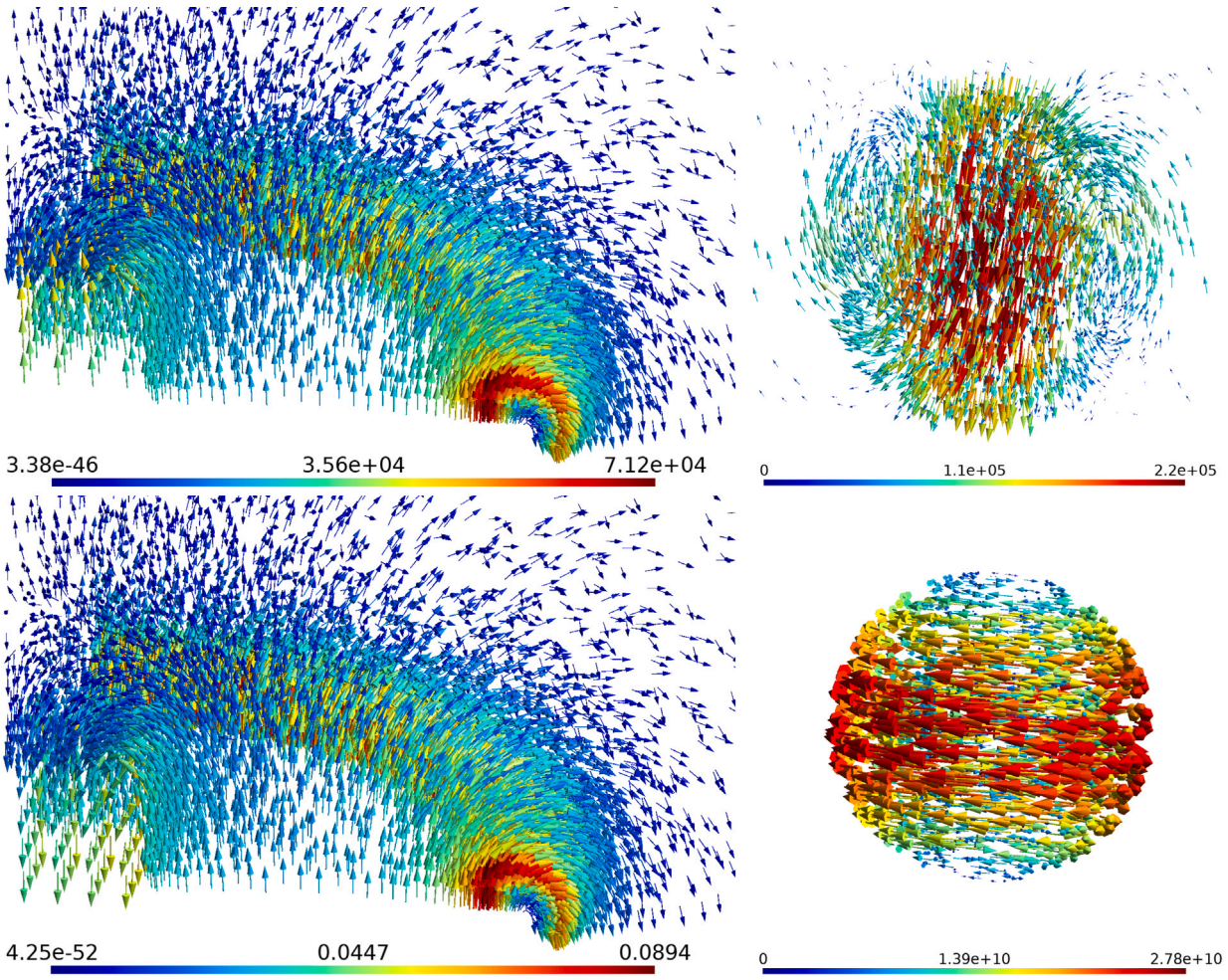

Fig. 9. Field maps of homogenized macroscopic $\boldsymbol{H}$ (top left), homogenized macroscopic $\boldsymbol{B}$ (bottom left), fine-scale magnetic field distribution $\boldsymbol{h}$ (top right) and fine-scale induced currents $\boldsymbol{j}$ (bottom right) in the corner cell problem, at time step 81 of the HMM resolution using the linear parameters from Table 2. This time step corresponds to the time when $\boldsymbol{J}_s$ and $\boldsymbol{H}$ reverse sign, $\boldsymbol{B}$ is small and $\partial_t \boldsymbol{B}$ / $\boldsymbol{j}$ / $\boldsymbol{m}_{l\to \mathrm{H}}$ are the highest. Due to the dynamic magnetization of the spheres, $\boldsymbol{B}$ lags behind $\boldsymbol{H}$ and points in the opposite direction in the core (bottom left in the macroscopic field maps) due to the strong dynamic magnetization $\boldsymbol{M}_{l\to \mathrm{H}}$. This is visible in the cell: the average of $\boldsymbol{h} = \nu_0 \boldsymbol{b}$ in the whole cell points down, but outside the sphere and especially tangentially to the cell boundary, it points up. Since $\boldsymbol{\nu} = \nu_0 I_3$ here, $\boldsymbol{M}_{\bullet \to l}$ is zero so the macroscopic magnetization $\boldsymbol{M}$ is only due to the fine-scale eddy currents.

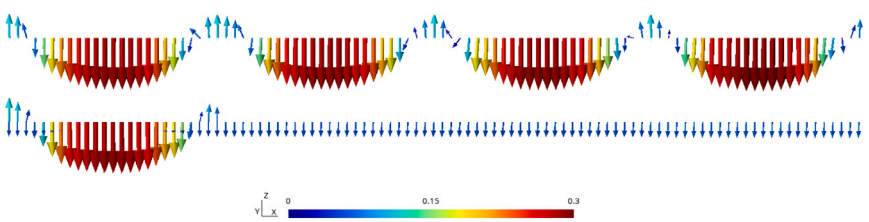

Fig. 10. Cut of the magnetic field in the core on a line in the $\boldsymbol{e}_x$ direction, through the center of the innermost inclusion and its neighbors, at TS 81 as in Fig. 9. The reference solution $\boldsymbol{b}^l$ is at the top, while the macroscopic field $\boldsymbol{B}$ and the magnetic field in the innermost cell $\boldsymbol{b}$ are at the bottom, the scale is in Tesla. The local fields qualitatively match. Remark: this macroscopic $\boldsymbol{B}$ is the cell average of $\boldsymbol{b}$, not the average of the displayed part of $\boldsymbol{b}$ (that is only on a line).

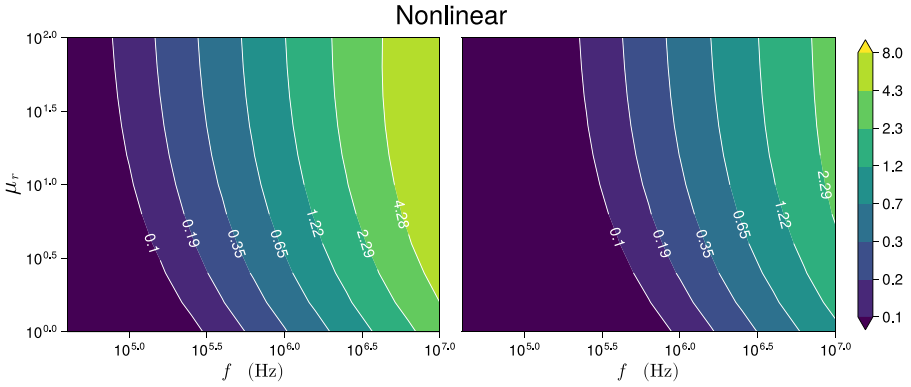

Fig. 11. Log–log map of the average over one period of $100H_{\text{err}}$ ($\boldsymbol{M}_{l\to\text{H}}$-$\boldsymbol{H}$ ratio (33), left) and $100\sqrt{P_{\text{rat}}}$ ($\mathcal{P}_{\text{JL}}$-$\mathcal{P}_{\text{em}}$ ratio (34), right), for different frequencies and maximum magnetic relative permeability, in the cell with nonlinear magnetic law. Both maps follow the same trend, but unlike with linear material law [24][30, Fig. 3.12], the power ratio underestimates the dynamic magnetization share in the upscaled magnetic field.

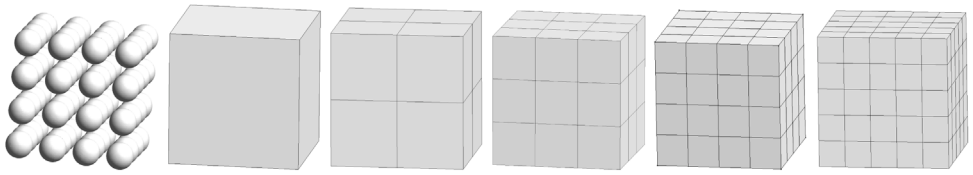

Fig. 12. Geometry (leftmost) and homogenized domain meshes (right) used to study convergence of FE-HMM with macroscopic mesh refinement.

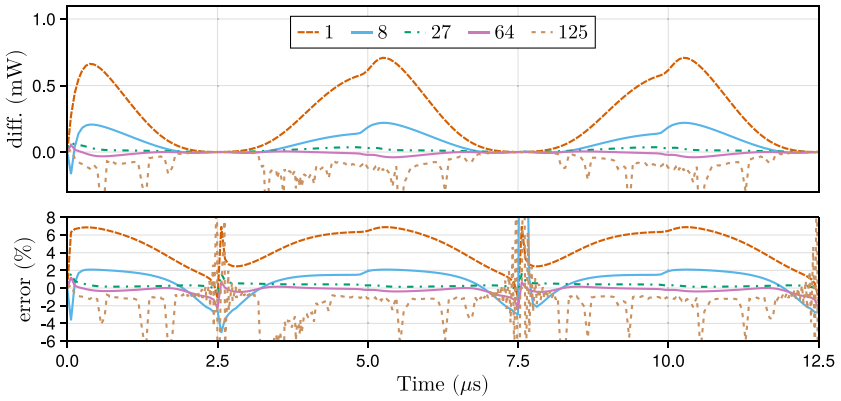

Fig. 13. Instantaneous relative error (top) and percentage of error (bottom) in EC losses prediction of FE-HMM for different homogenized domain meshes. The error converges and decreases, until the multiscale convergence becomes unstable (for 125 macroscopic elements/bottom curve).

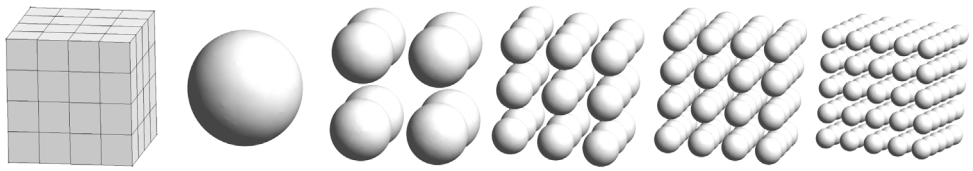

Fig. 14. Homogenized domain mesh (leftmost) and core geometries (right) used to study convergence of HMM with the scale separation parameter l (cell size).

Table 8
Percentage of error on EC losses and electromagnetic power prediction by HMM for the geometries in Fig. 14, integrated over the whole simulation time. Excellent agreement with reference is reached.

Linear $\mathcal{P}_{\mathrm{JL}}$					
l (μm)	400	200	133	100	80
L^2_{Err} (%)	6.14	1.18	0.40	0.71	0.33

Linear $\mathcal{P}_{\mathrm{em}}$					
l (μm)	400	200	133	100	80
L^2_{Err} (%)	3.22	0.27	0.07	0.50	0.56

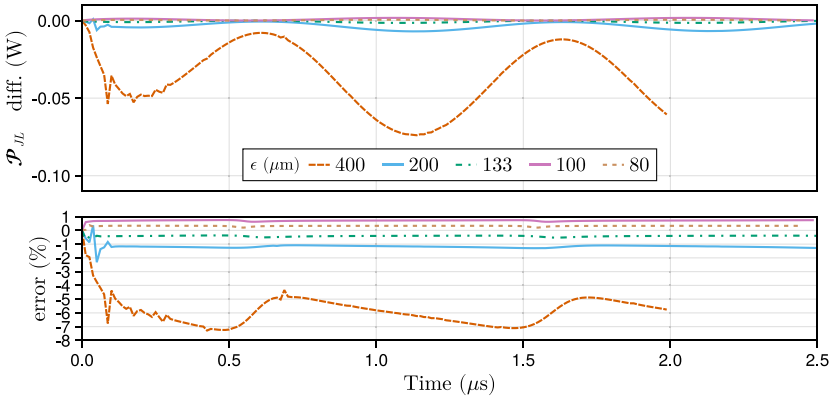

Fig. 15. Instantaneous relative error (top) and percentage of error (bottom) in EC losses prediction of HMM for cell sizes (from 400 μm to 80 μm, c.f. Fig. 14). The error converges and decreases steadily, excellent agreement with the reference is reached.

Convergence of the modeling error

Using a two-scale FE-HMM induces a modeling error by assuming a scale separation hypothesis and replacing the given problem by a two-scale problem. The next test aims to confirm that this error decreases with the number of spatial periods in the geometry.

Five different cores with a fixed width of 800 μm are simulated, each containing 8, 64, 216, 512 and 1000 balls (this corresponds to cell sizes of $l = 400$, 200, 133, 100 and 80 μm respectively), the macroscopic mesh and core geometries are shown in Fig. 14. The figure also illustrates that the macroscopic mesh does not have to match the physical periods of the heterogeneous domain, the cells are sometimes bigger or smaller than the macroscopic element in these resolutions. A linear magnetic law with $\mu_{\mathrm{r}} = 100$ is used in the balls to reduce the computational cost, a conductivity $\sigma = 10 \times 10^6$ S.m^{-1} and frequency $f = 500$ kHz.

Since the cores differ, solutions are not expected to match. Therefore, errors are computed relative to a core-specific reference solution. The EC losses errors are plotted in Fig. 15, and the integrated errors are in Table 8. The convergence is very good until the error becomes small and stagnates. This stagnation is presumably caused by the modeling error becoming comparable to the discretization error.

Simulation beyond the capabilities of single scale FEM

A last experiment is run to illustrate the ability of the multiscale method to handle problems impossible to solve with a single scale FEM. The nonlinear test case ($f = 100$ MHz, $I = 800$ A, $\langle h \rangle_{\partial Y_\parallel}$ upscaling) is solved again on two other heterogeneous domains obtained by reducing the cell width to 10 μm and 6.66 μm. This corresponds to 512 000 and 1 728 000 balls in the magnetic core, making it impossible to compute reference solutions on a fine-scale mesh. However, the macroscopic mesh is the same as in the previous experiment (Fig. 14 left): it has 64 coarse elements in Ω_{H} and thus uses only 64 cell problems. The computational complexity is independent of the cell size and real number of inclusions, which is the great advantage of FE-HMM.

The obtained EC losses estimations are plotted in Fig. 16 and they evolve as expected. The numerical multiscale convergence being very good, and given that the previous experiment demonstrated excellent convergence of the homogenization error (Fig. 15), it seems reasonable to consider the results be accurate.

6. Conclusions

This paper develops a multiscale B-conforming formulation of the magneto-quasi-static problem on periodic materials featuring magnetic and conducting inclusions that are electrically insulated from each other. The method combines the heterogeneous multiscale method with first order finite element spatial discretization and a time stepping scheme.

The crux of the method is the homogenization of the magnetic field strength, that needs to take into account the presence of strong eddy currents and associated dynamic magnetization. The formulations fit into the framework recently derived by Wulfinghoff [29], in the particular case of periodic media. To do so, five existing methods for magnetic field strength upscaling were reviewed, and a new method was proposed. This new method uses a FEM projection to compute the periodic correction field that would be solution of the H-conforming cell problem. The boundary tangential average method seems to be the best compromise of numerical stability and efficiency.

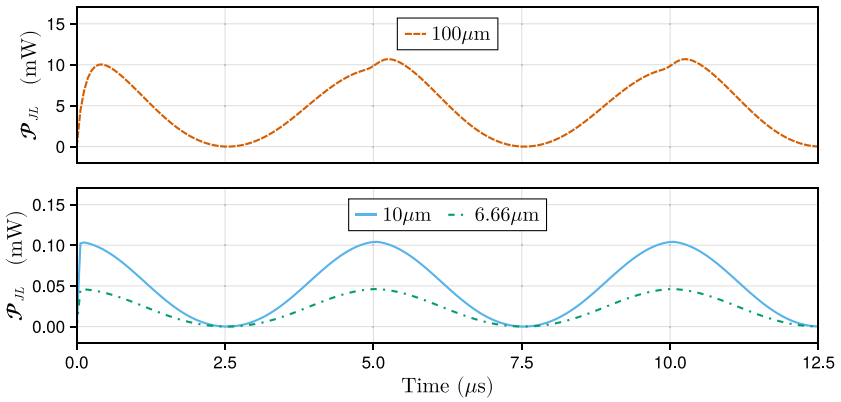

Fig. 16. EC losses prediction by HMM for a core of total width 800 μm with cell sizes of 100, 10 and 6.66 μm. As expected, the EC losses decrease with the square of the inclusion radius. The self-inductance and transient effects due to dynamic magnetization also decrease.

We validated the multiscale B-conforming HMM formulation on 3D linear and nonlinear problems, demonstrating an excellent accuracy with approximately 1% of error on the total Joule losses, by comparison with a standard single scale FEM formulation. The method accuracy is robust to strong dynamic hysteresis emerging in the macroscopic magnetic law. Additionally, a good convergence of the discretization and modeling errors is numerically demonstrated. Finally, the method was applied to a problem impossible to solve with standard FEM, illustrating its capabilities.

Further developments seem necessary for industrial uses. The numerical stability of the weak coupling between both scales is to be better understood and improved. Also, handling thousands of homogenized domain macroscopic elements would require the resolution cost for solving the cell problems to be reduced. This could be achieved using model order reduction techniques, or hysteresis material models fitted using the solutions of the cell problem, for example.

CRediT authorship contribution statement

Antoine Marteau: Writing – original draft, Visualization, Software, Methodology, Investigation, Formal analysis, Conceptualization. **Innocent Niyonzima:** Writing – review & editing, Supervision, Software, Methodology, Funding acquisition, Formal analysis, Conceptualization. **Janne Ruuskanen:** Writing – review & editing, Methodology. **Gérard Meunier:** Writing – review & editing, Supervision, Methodology, Conceptualization. **Nicolas Galopin:** Writing – review & editing, Supervision, Methodology. **Timo Tarhasaari:** Writing – review & editing. **Paavo Rasilo:** Writing – review & editing. **Olivier Chadebec:** Writing – review & editing, Supervision, Project administration, Methodology.

Declaration of competing interest

The authors declare that they have no known competing financial interests or personal relationships that could have appeared to influence the work reported in this paper.

Acknowledgments

This work was supported by IDEX Université Grenoble Alpes under the Strategic Research Initiatives (IRS) funding scheme which funded the PhD research work of the first author.

We warmly thank the anonymous reviewers for their numerous, relevant and detailed comments, that significantly contributed to the clarity and quality of this paper.

Appendix

A.1. Inverse Fröhlich–Kennelly nonlinear magnetic law

The analytic inverse of the $\boldsymbol{b}(\boldsymbol{h})$ law (28) is the $\boldsymbol{h}(\boldsymbol{b})$ law defined by the reluctivity

$$\nu(\boldsymbol{b}) = \frac{2B_s}{c_1(\|\boldsymbol{b}\|) + c_2(\|\boldsymbol{b}\|)} \tag{35}$$

with

$$c_1(\|\boldsymbol{b}\|) = \mu_0\mu_r^{\max}B_s - \mu_0(\mu_r^{\max}-1)\|\boldsymbol{b}\|, \quad c_2(\|\boldsymbol{b}\|) = \sqrt{c_1(\|\boldsymbol{b}\|)^2 + c_3\|\boldsymbol{b}\|} \text{ and } c_3 = 4B_s\mu_0^2(\mu_r^{\max}-1).$$

The Jacobian matrix of the law is given by

$$\frac{\partial \boldsymbol{h}}{\partial \boldsymbol{b}}(\boldsymbol{b}) = \nu(\boldsymbol{b}) I_3 + \frac{1}{\|\boldsymbol{b}\|}\frac{\partial \nu(\boldsymbol{b})}{\partial \|\boldsymbol{b}\|}\boldsymbol{b}\otimes\boldsymbol{b} \tag{36}$$

where

$$\frac{\partial \nu(\boldsymbol{b})}{\partial \|\boldsymbol{b}\|} = \frac{\mu_0}{2}(\mu_{\mathrm{r}}^{\max}-1)\nu(\boldsymbol{b})^2 + \frac{1}{B_{\mathrm{s}}}\left(1 + \frac{c_1(\|\boldsymbol{b}\|) - 4B_{\mathrm{s}}\mu_0}{c_2(\|\boldsymbol{b}\|)}\right). \tag{37}$$

It can be verified that $\boldsymbol{h}(\boldsymbol{b})$ is equivalent to $\frac{1}{\mu_0\mu_{\mathrm{r}}^{\max}}\boldsymbol{b}$ near $\|\boldsymbol{b}\| = 0$ and to $\frac{1}{\mu_0}\boldsymbol{b}$ for $\|\boldsymbol{b}\| \gg B_{\mathrm{s}}$.

A.2. Numerical B-conforming reference formulation

In the rest of the Appendix, the superscript $\bullet^{n+1}$ is dropped for clarity, but all quantities that are not labeled $\bullet^n$ are quantities at time $n+1$.

The discrete weak formulation of the reference problem (6) with explicit time and NL discretization, at time step $n+1$ and NL iteration $K+1$, is: find $\boldsymbol{a} \in \boldsymbol{H}_{h,\boldsymbol{0}_\tau,\boldsymbol{0}\Gamma_b}(\mathbf{curl};\Omega)$ and $v \in H_h(\mathbf{grad};\Omega_{\mathrm{C}})\backslash\mathbb{R}^{\beta_{0,\mathrm{C}}}$ s.t.

$$\begin{aligned}\int_{\Omega_{l,\mathrm{N},h}} \frac{1}{\mu_0}\cdot\mathbf{curl}\,\boldsymbol{a}\cdot\mathbf{curl}\,\boldsymbol{a}' + \int_{\Omega_{l,\mathrm{C},h}}\left(\boldsymbol{h}(\boldsymbol{b}^K) + \frac{\partial \boldsymbol{h}}{\partial \boldsymbol{b}}(\boldsymbol{b}^K)\cdot\mathbf{curl}\,(\boldsymbol{a}-\boldsymbol{a}^K)\right)\cdot\mathbf{curl}\,\boldsymbol{a}' \\ + \int_{\Omega_{l,\mathrm{C},h}}\sigma\Big(\frac{1}{\Delta t}(\boldsymbol{a}-\boldsymbol{a}^n) + \mathbf{grad}\,v\Big)\cdot\boldsymbol{a}' = \int_{\Omega_{\mathrm{s},h}}\boldsymbol{j}_{\mathrm{s}}\cdot\boldsymbol{a}' \\ \text{and}\quad \int_{\Omega_{l,\mathrm{C},h}}\sigma\Big(\frac{1}{\Delta t}(\boldsymbol{a}-\boldsymbol{a}^n) + \mathbf{grad}\,v\Big)\cdot\mathbf{grad}\,v' = 0,\end{aligned} \tag{38}$$

for all $\boldsymbol{a}' \in \boldsymbol{H}_{h,\boldsymbol{0}_\tau,\boldsymbol{0}\Gamma_b}(\mathbf{curl};\Omega)$ and $v' \in H_h(\mathbf{grad};\Omega_{\mathrm{C}})\backslash\mathbb{R}^{\beta_{0,\mathrm{C}}}$, where $\boldsymbol{b}^K = \mathbf{curl}\,\boldsymbol{a}^K$ is the magnetic induction at the previous nonlinear iteration and $\boldsymbol{a}^n$ is the solution at the previous time step. Relaxing the nonlinear loop was not needed, so the solution at the next iteration is simply $\boldsymbol{a}^{K+1} = \boldsymbol{a}$ the solution of (38).

A.3. Numerical B-conforming two-scale HMM formulation

The discrete weak formulation of the cell problem (22), at time step $n+1$, macro iteration $K+1$ and cell iteration $k+1$, is: find $\boldsymbol{a}_{\mathrm{c}} \in \boldsymbol{H}^{\#}_{h,\boldsymbol{0}\gamma_Y}(\mathbf{curl};Y)$ and $\xi_{\mathrm{p}} \in H^{\#}_{h,0\partial Y_{\mathrm{C}}}(\mathbf{grad};Y_{\mathrm{N}})$ s.t.

$$\begin{aligned}\int_{Y_{\mathrm{C},h}}\left(\boldsymbol{h}(\boldsymbol{b}^k) + \frac{\partial \boldsymbol{h}}{\partial \boldsymbol{b}}(\boldsymbol{b}^k)\cdot\mathbf{curl}\,(\boldsymbol{a}_{\mathrm{c}} - \boldsymbol{a}_{\mathrm{c}}^k)\right)\cdot\mathbf{curl}\,\boldsymbol{a}_{\mathrm{c}}' + \int_{Y_{\mathrm{C},h}}\sigma\Big(\frac{1}{\Delta t}(\boldsymbol{a}_{\mathrm{c}} - \boldsymbol{a}_{\mathrm{c}}^n) + \frac{1}{2}\partial_t\boldsymbol{B}^K\times\boldsymbol{y}\Big)\cdot\boldsymbol{a}_{\mathrm{c}}' \\ + \int_{Y_{\mathrm{N},h}}\frac{1}{\mu_0}(\boldsymbol{B}^K + \mathbf{curl}\,\boldsymbol{a}_{\mathrm{c}})\cdot\mathbf{curl}\,\boldsymbol{a}_{\mathrm{c}}' + \int_{Y_{\mathrm{N},h}}\lambda_1\mathbf{grad}\,\xi_{\mathrm{p}}\cdot\boldsymbol{a}_{\mathrm{c}}' = 0,\end{aligned} \tag{39}$$

$$\int_{Y_{\mathrm{N},h}}\lambda_1\boldsymbol{a}_{\mathrm{c}}\cdot\mathbf{grad}\,\xi_{\mathrm{p}}' + \lambda_2\xi_{\mathrm{p}}\xi_{\mathrm{p}}' = 0$$

for all $\boldsymbol{a}_{\mathrm{c}}' \in \boldsymbol{H}^{\#}_{h,\boldsymbol{0}\gamma_Y}(\mathbf{curl};Y)$ and $\xi_{\mathrm{p}}' \in \boldsymbol{H}^{\#}_{h,0\partial Y_{\mathrm{C}}}(\mathbf{grad};Y_{\mathrm{N}})$, where $\boldsymbol{b}^k = \boldsymbol{B}^K + \mathbf{curl}\,\boldsymbol{a}_{\mathrm{c}}^k$ is the magnetic induction at the previous nonlinear iteration, $\boldsymbol{a}_{\mathrm{c}}^n$ is the solution at the previous time step and $\partial_t\boldsymbol{B}^K = \frac{1}{\Delta t}(\boldsymbol{B}^K - \boldsymbol{B}^n)$. Relaxing the nonlinear cell loop was not needed, so the solution at the next iteration is simply $\boldsymbol{a}_{\mathrm{c}}^{k+1} = \boldsymbol{a}_{\mathrm{c}}$ the solution of (39).

After convergence of the cell problem at iteration k_{F}, $\boldsymbol{a}_{\mathrm{c}}^{K+1} = \boldsymbol{a}_{\mathrm{c}}^{k_{\mathrm{F}}}$ is obtained, as well as $\boldsymbol{b}^{K+1} = \boldsymbol{B}^K + \mathbf{curl}\,\boldsymbol{a}_{\mathrm{c}}^{K+1}$, $\boldsymbol{h}^{K+1} = \boldsymbol{h}(\boldsymbol{b}^{K+1})$ and the upscaled quantities to compute from these.

To solve the perturbed cell problems in order to compute $\frac{\partial \boldsymbol{H}}{\partial \boldsymbol{B}}^{K+1}$ (c.f. (18)), $\boldsymbol{a}_{\mathrm{c}}^{i,k=0}$ is initialized with $\boldsymbol{a}_{\mathrm{c}}^{K+1}$ the solution of the unpertubed cell problem, and iteratively solve (39) with $\boldsymbol{B}^K + \eta\boldsymbol{e}_i$ in place of $\boldsymbol{B}^K$, for $i = \{x, y, z\}$.

A.4. Computation of the cell magnetization

To derive the discrete weak form of (26), the terms $\boldsymbol{a}$ and $\boldsymbol{B}$ are replaced with their discrete solution from (39), to obtain: find $\widetilde{\boldsymbol{m}_{l\to\mathrm{H}}}^{K+1} \in \boldsymbol{H}_{h,\boldsymbol{0}}(\mathbf{curl};Y_{\mathrm{C}})$ and $\xi \in H_{h,0}(\mathbf{grad};Y_{\mathrm{C}})$ such that

$$\begin{aligned}\int_{Y_{\mathrm{C},h}}\left(\mathbf{curl}\,\widetilde{\boldsymbol{m}_{l\to\mathrm{H}}}^{K+1} - \frac{\sigma}{\Delta t}\Big(\boldsymbol{a}_{\mathrm{c}}{}^{K+1} - \boldsymbol{a}_{\mathrm{c}}^n + \frac{1}{2}(\boldsymbol{B}^K - \boldsymbol{B}^n)\times\boldsymbol{y}\Big)\right)\cdot\mathbf{curl}\,\boldsymbol{m}' + \int_{Y_{\mathrm{C},h}}\mathbf{grad}\,\xi\cdot\boldsymbol{m}' = 0 \\ \int_{Y_{\mathrm{C},h}}\widetilde{\boldsymbol{m}_{l\to\mathrm{H}}}^{K+1}\cdot\mathbf{grad}\,\xi' + \xi\xi' = 0\end{aligned} \tag{40}$$

for all $\boldsymbol{m}' \in \boldsymbol{H}_{h,\boldsymbol{0}}(\mathbf{curl};Y_{\mathrm{C}})$ and $\xi' \in H_{h,0}(\mathbf{grad};Y_{\mathrm{C}})$, where $\widetilde{\boldsymbol{m}_{l\to\mathrm{H}}}^{K+1}$ was gauged using the Coulomb gauge. After the resolution, $\boldsymbol{H}^{K+1} = \left\langle \boldsymbol{h}^{K+1} - \widetilde{\boldsymbol{m}_{l\to\mathrm{H}}}^{K+1}\right\rangle_Y$ can be computed.

A.5. Computation of magnetic field strength correction

The derivation of the discrete weak form of (27) is similar to that of (40), leading to: find $\widetilde{\boldsymbol{h}_{\mathrm{c}}}^{K+1} \in \boldsymbol{H}^{\#}_{h,\mathbf{0}\boldsymbol{\gamma}_Y}(\mathbf{curl};Y)$ and $\xi_{\mathrm{c}} \in H^{\#}_{h,0\mathrm{P}_Y}(\mathbf{grad};Y)$ such that

$$\begin{aligned}\int_{Y_h}\left(\mathbf{curl}\,\widetilde{\boldsymbol{h}_{\mathrm{c}}}^{K+1}-\frac{\sigma}{\Delta t}\left(\boldsymbol{a}_{\mathrm{c}}{}^{K+1}-\boldsymbol{a}_{\mathrm{c}}^{n}+\frac{1}{2}(\boldsymbol{B}^{K}-\boldsymbol{B}^{n})\times\boldsymbol{y}\right)\right)\cdot\mathbf{curl}\,\boldsymbol{h}_{\mathrm{p}}{}'+\int_{Y_h}\mathbf{grad}\,\xi_{\mathrm{c}}\cdot\boldsymbol{h}_{\mathrm{p}}{}'=0,\\ \int_{Y_h}\widetilde{\boldsymbol{h}_{\mathrm{c}}}^{K+1}\cdot\mathbf{grad}\,\xi_{\mathrm{c}}{}'+\xi_{\mathrm{c}}\xi_{\mathrm{c}}{}'=0,\end{aligned}\tag{41}$$

for all $\boldsymbol{h}_{\mathrm{p}}{}' \in \boldsymbol{H}^{\#}_{h,\mathbf{0}\boldsymbol{\gamma}_Y}(\mathbf{curl};Y)$ and $\xi_{\mathrm{c}}{}' \in H^{\#}_{h,0\mathrm{P}_Y}(\mathbf{grad};Y)$, where $\widetilde{\boldsymbol{h}_{\mathrm{c}}}^{K+1}$ was gauged using the Coulomb gauge. After the resolution, $\boldsymbol{H}^{K+1}=\left\langle \boldsymbol{h}^{K+1}-\widetilde{\boldsymbol{h}_{\mathrm{c}}}^{K+1}\right\rangle_Y$ can be computed. The space $H^{\#}_{h,0\mathrm{P}_Y}(\mathbf{grad};Y)$ is the space of periodic scalar potentials equal to zero at the cell corners:

$$H^{\#}_{h,0\mathrm{P}_Y}(\mathbf{grad};Y)=\left\{\upsilon_{\mathrm{c}}\in H^{\#}_{h}(\mathbf{grad};Y)\quad\middle|\quad \upsilon_{\mathrm{c}}\big|_{\mathrm{P}_Y}=0\right\}.\tag{42}$$

Data availability

No data was used for the research described in the article.

References

[1] T.C. Choy, Effective Medium Theory: Principles and Applications, Oxford University Press, 2015, http://dx.doi.org/10.1093/acprof:oso/9780198705093.001.0001.

[2] A.H. Sihvola, Electromagnetic mixing formulas and applications, in: Electromagnetic Waves, IET, 1999, http://dx.doi.org/10.1049/PBEW047E.

[3] X. Ren, Modélisation semi-analytique des pertes par courants de Foucault dans les matériaux composites (Ph.D. thesis), Université Paris-Saclay (ComUE), 2017, URL: https://www.theses.fr/2017SACLS159.

[4] T.Y. Hou, X.-H. Wu, A multiscale finite element method for elliptic problems in composite materials and porous media, J. Comput. Phys. 134 (1) (1997) 169–189.

[5] J. Fish, Practical Multiscaling, John Wiley & Sons, 2013, URL: https://www.wiley.com/en-us/Practical+Multiscaling-p-9781118410684.

[6] O. Bottauscio, A. Manzin, Comparison of multiscale models for eddy current computation in granular magnetic materials, J. Comput. Phys. 253 (2013) 1–17.

[7] O. Bottauscio, M. Chiampi, A. Manzin, Multiscale modeling of heterogeneous magnetic materials, Int. J. Numer. Modelling, Electron. Netw. Devices Fields 27 (3) (2014) 373–384.

[8] I. Niyonzima, Multiscale Finite Element Modeling of Nonlinear Quasistatic Electromagnetic Problems (Ph.D. thesis), 2014, URL: https://orbi.uliege.be/handle/2268/171929.

[9] T.J.R. Hughes, Multiscale phenomena: Green's functions, the Dirichlet-to-Neumann formulation, subgrid scale models, bubbles and the origins of stabilized methods, Comput. Methods Appl. Mech. Engrg. 127 (1) (1995) 387–401.

[10] B. Verfürth, Numerical multiscale methods for waves in high-contrast media, Jahresber. Dtsch. Mathematiker-Vereinigung 126 (1) (2024) 37–65.

[11] A. Abdulle, E. Weinan, B. Engquist, E. Vanden-Eijnden, The heterogeneous multiscale method, Acta Numer. 21 (2012) 1–87.

[12] W. Ee, B. Engquist, X. Li, W. Ren, E. Vanden-Eijnden, Heterogeneous multiscale methods: A review, Commun. Comput. Phys. 2 (2007).

[13] J. Schröder, A numerical two-scale homogenization scheme: the FE2-method, in: J. Schröder, K. Hackl (Eds.), Plasticity and beyond: Microstructures, Crystal-Plasticity and Phase Transitions, Springer, 2014, pp. 1–64, http://dx.doi.org/10.1007/978-3-7091-1625-8_1.

[14] A. Bossavit, On the homogenization of Maxwell equations, COMPEL- Int. J. Comput. Math. Electr. Electron. Eng. 14 (4) (1995) 23–26.

[15] M. El Feddi, Z. Ren, A. Razek, A. Bossavit, Homogenization technique for Maxwell equations in periodic structures, IEEE Trans. Magn. 33 (2) (1997) 1382–1385.

[16] G. Meunier, V. Charmoille, C. Guerin, P. Labie, Y. Marechal, Homogenization for periodical electromagnetic structure: Which formulation? IEEE Trans. Magn. 46 (8) (2010) 3409–3412.

[17] P. Ciarlet Jr., S. Fliss, C. Stohrer, On the approximation of electromagnetic fields by edge finite elements. Part 2: A heterogeneous multiscale method for Maxwell's equations, Comput. Math. Appl. 73 (9) (2017) 1900–1919.

[18] O. Ouchetto, C.-W. Qiu, S. Zouhdi, L.-W. Li, A. Razek, Homogenization of 3-D periodic bianisotropic metamaterials, IEEE Trans. Microw. Theory Tech. 54 (11) (2006) 3893–3898.

[19] L. Cao, K. Li, J. Luo, Y. Wong, A multiscale approach and a hybrid FE-FDTD algorithm for 3D time-dependent Maxwell's equations in composite materials, Multiscale Model. Simul. 13 (4) (2015) 1446–1477.

[20] O. Bottauscio, V.C. Piat, M. Chiampi, M. Codegone, A. Manzin, Nonlinear homogenization technique for saturable soft magnetic composites, IEEE Trans. Magn. 44 (11) (2008) 2955–2958.

[21] I. Niyonzima, R.V. Sabariego, P. Dular, F. Henrotte, C. Geuzaine, Computational homogenization for laminated ferromagnetic cores in magnetodynamics, IEEE Trans. Magn. 49 (5) (2013) 2049–2052.

[22] I. Niyonzima, R.V. Sabariego, P. Dular, C. Geuzaine, Nonlinear computational homogenization method for the evaluation of eddy currents in soft magnetic composites, IEEE Trans. Magn. 50 (2) (2014) 61–64.

[23] I. Niyonzima, R.V. Sabariego, P. Dular, K. Jacques, C. Geuzaine, Multiscale finite element modeling of nonlinear magnetoquasistatic problems using magnetic induction conforming formulations, Multiscale Model. Simul. 16 (1) (2018) 300–326.

[24] A. Marteau, I. Niyonzima, G. Meunier, J. Ruuskanen, N. Galopin, P. Rasilo, O. Chadebec, Magnetic field upscaling and B-conforming magnetoquasistatic multiscale formulation, IEEE Trans. Magn. 59 (5) (2023) 1–4.

[25] J. Ruuskanen, A. Marteau, I. Niyonzima, A. Halbach, J. Vesa, G. Meunier, T. Tarhasaari, P. Rasilo, Multiharmonic multiscale modelling in 3-D nonlinear magnetoquasistatics: Composite material made of insulated particles, Comput. Methods Appl. Mech. Engrg. 425 (2024).

[26] I. Niyonzima, G. Meunier, A. Marteau, R.V. Sabariego, O. Chadebec, N. Galopin, C. Geuzaine, Magnetic field conforming multiscale formulations for locally-confined nonlinear eddy current problems using the FE-HMM method, 2025, (in revision).

[27] J. Pendry, A. Holden, D. Robbins, W. Stewart, Magnetism from conductors and enhanced nonlinear phenomena, IEEE Trans. Microw. Theory Tech. 47 (11) (1999) 2075–2084.
[28] A.K. Amert, V.V. Gozhenko, K.W. Whites, Calculation of effective material parameters by field averaging over lattices with non-negligible unit cell size, Appl. Phys. A 109 (4) (2012) 1007–1013.
[29] S. Wulfinghoff, Variationally consistent magnetodynamic computational homogenization of particulate composites using an incremental potential, Comput. Methods Appl. Mech. Engrg. 432 (2024) 117421.
[30] A. Marteau, Multiscale Models for Nonlinear Transient Electromagnetic Problems with Confined Eddy Currents (Ph.D. thesis), (2024GRALT019) Université Grenoble Alpes, 2024, URL: https://theses.hal.science/tel-04603453.
[31] R.V. Kohn, S.P. Shipman, Magnetism and homogenization of micro-resonators, Multiscale Model. Simul. 7 (1) (2007) 62–92.
[32] B. Schweizer, M. Urban, Effective Maxwell's equations in general periodic microstructures, Appl. Anal. 97 (13) (2018) 2210–2230.
[33] A.A. Rodríguez, A. Valli, Eddy Current Approximation of Maxwell Equations_ Theory, Algorithms and Applications, Springer-Verlag Italia, 2010.
[34] D.J. Griffiths, Introduction to Electrodynamics, fourth ed. Cambridge University Press, 2017.
[35] A. Kameari, Calculation of transient 3D eddy current using edge-elements, IEEE Trans. Magn. 26 (2) (1990) 466–469.
[36] E. Creusé, P. Dular, S. Nicaise, About the gauge conditions arising in finite element magnetostatic problems, Comput. Math. Appl. 77 (6) (2019) 1563–1582.
[37] P. Monk, Finite element methods for Maxwell's equations, in: Numerical mathematics and scientific computation, Oxford University Press, Oxford, 2003, http://dx.doi.org/10.1093/acprof:oso/9780198508885.001.0001.
[38] H.A. Lorentz, The Theory of Electrons and Its Applications to the Phenomena of Light and Radiant Heat, G.E. Stechert, Leipzig, 1916, B.G. Teubner ; New York, URL: http://archive.org/details/electronstheory00lorerich.
[39] G. Russakoff, A derivation of the macroscopic Maxwell equations, Am. J. Phys. 38 (10) (1970) 1188–1195.
[40] C. Vassallo, Electromagnétisme classique dans la matiere, Dunod, 1980.
[41] K. Hollaus, J. Schöberl, Some 2-D multiscale finite-element formulations for the eddy current problem in iron laminates, IEEE Trans. Magn. 54 (4) (2018) 1–16.
[42] G. Nguetseng, A general convergence result for a functional related to the theory of homogenization, SIAM J. Math. Anal. 20 (3) (1989) 608–623.
[43] G. Allaire, Homogenization and two-scale convergence, SIAM J. Math. Anal. 23 (6) (1992) 1482–1518.
[44] A. Visintin, Electromagnetic processes in doubly-nonlinear composites, Comm. Partial Differential Equations 33 (2008) 808–841.
[45] A. Visintin, Homogenization of a parabolic model of ferromagnetism, J. Differential Equations 250 (3) (2011) 1521–1552.
[46] Y. Amirat, V. Shelukhin, Homogenization of time harmonic Maxwell equations and the frequency dispersion effect, J. Math. Pures Appl. 95 (4) (2011) 420–443.
[47] Y. Amirat, V.V. Shelukhin, Homogenization of time harmonic Maxwell equations: the effect of interfacial currents, Math. Methods Appl. Sci. 40 (8) (2017) 3140–3162.
[48] G. Bouchitté, D. Felbacq, Homogenization near resonances and artificial magnetism from dielectrics, Comptes Rendus Math. 339 (5) (2004) 377–382.
[49] G. Bouchitté, D. Felbacq, Homogenization of a wire photonic crystal: The case of small volume fraction, SIAM J. Appl. Math. 66 (6) (2006) 2061–2084.
[50] G. Bouchitté, C. Bourel, D. Felbacq, Homogenization of the 3D Maxwell system near resonances and artificial magnetism, Comptes Rendus Math. 347 (9–10) (2009) 571–576.
[51] G. Bouchitté, C. Bourel, D. Felbacq, Homogenization near resonances and artificial magnetism in three dimensional dielectric metamaterials, Arch. Ration. Mech. Anal. 225 (3) (2017) 1233–1277.
[52] B. Verfürth, Heterogeneous multiscale method for the Maxwell equations with high contrast, ESAIM: Math. Model. Numer. Anal. 53 (1) (2019) 35–61.
[53] M. Ohlberger, B. Verfurth, A new heterogeneous multiscale method for the Helmholtz equation with high contrast, Multiscale Model. Simul. 16 (1) (2018) 385–411.
[54] M. Ohlberger, B. Schweizer, M. Urban, B. Verfürth, Mathematical analysis of transmission properties of electromagnetic meta-materials, 2018, http://dx.doi.org/10.48550/arXiv.1809.08824.
[55] D. Felbacq, G. Bouchitté, Homogenization of a set of parallel fibres, Waves Random Media 7 (2) (1997).
[56] G. Bouchitté, B. Schweizer, Homogenization of Maxwell's equations in a split ring geometry, Multiscale Model. Simul. 8 (2010) 717–750.
[57] M.M. Ameen, R.H.J. Peerlings, M.G.D. Geers, A quantitative assessment of the scale separation limits of classical and higher-order asymptotic homogenization, Eur. J. Mech. A Solids 71 (2018) 89–100.
[58] M. Fergoug, A. Parret-Fréaud, N. Feld, B. Marchand, S. Forest, Hierarchical modeling of heterogeneous structures driven by a modeling error estimator, Comput. Methods Appl. Mech. Engrg. 418 (2024).
[59] R.M. Bozorth, Ferromagnetism, in: Bell Telephone Laboratories series, Van Nostrand, 1951.
[60] GRICAD, URL: https://gricad.univ-grenoble-alpes.fr/index.html.
[61] Nic5, URL: https://www.ceci-hpc.be/clusters.html#nic5.